Experimental study of chlorite authigenesis and influence on porosity maintenance in sandstones

Dimitrios Charlaftis[1], Stuart J. Jones[1], Katherine J. Dobson[2], Jonathan Crouch[3] and Sanem Acikalin[4]

[1]Department of Earth Sciences, Durham University, South Road, Durham, DH1 3LE, UK

[2]Department of Civil & Environmental Engineering, University of Strathclyde, G1 1XJ, UK

[3]BP, Chertsey Road, Sunbury on Thames, Middlesex, TW16 7BP, UK

[4]School of Natural and Environmental Sciences, Newcastle University, NE1 7RU, UK

e-mail: dimitrios.charlaftis@durham.ac.uk

Key words: chlorite coatings, berthierine transformation, siderite dissolution, diagenesis, reservoir quality

ABSTRACT

Chlorite is recognized as a key mineral for preserving reservoir quality in deeply buried sandstones, as chlorite coatings inhibit the nucleation of quartz overgrowths. A limited understanding of the mechanisms and conditions under which these authigenic chlorite coatings form prevents the accurate forward modeling of diagenesis and limits reservoir quality models critical to a wide range of geoscience applications. We present experimental data that show how authigenic chlorite grain coatings preserve porosity in deeply buried sandstone reservoirs, using a series of hydrothermal reactor experiments to simulate quartz cementation and capture the evolving porosity. To simulate reservoir evolution, berthierine-bearing sandstone samples (Lower Jurassic Cook Formation, Oseberg Field, 30/6-17R, Norway) were exposed to a silica-supersaturated Na_2CO_3 (0.1 M) solution for 72 hours at temperatures of between 100 and 250 °C. Quantification of the temperature-dependent changes in the volume of authigenic chlorite, the thickness and coverage of the clay coatings, and the sample porosity shows increases in chlorite volume (from ~ 2% to ~ 14%). This occurs by the transformation, of patchy amorphous berthierine into grain-coating Fe-chlorite cements through a mixture of the solid-state transformation and dissolution-precipitation mechanisms, siderite replacement, and direct precipitation on clay-free surfaces. With increasing temperature, the chlorite coatings increase from ~ 3.8 µm to ~ 5.4 µm thick and expand their grain surface coverage from ~ 28% to ~ 50%. The face-to-edge and face-to-face foliaceous structure of the clay coatings produced are morphologically similar to those observed in deeply buried sandstones. Only above temperatures of 175 °C is porosity preserved as a consequence of inhibition of quartz overgrowths and the generation of secondary porosity.

Our quantitative approach enhances our knowledge regarding the temperature and mineral precursor influence on chlorite-coating authigenesis and therefore provides key insight for chlorite grain coatings for reservoir potential in sedimentary sequences greater than 2.5 km.

INTRODUCTION

Quartz cementation is a major cause of porosity reduction in deeply buried sandstone reservoirs, typically initiating at temperatures of 80-100 °C and reducing both porosity and permeability during progressive burial (McBride 1989; Bjørlykke and Egeberg 1993; Worden and Morad 2000). However, quartz precipitation can be inhibited by the prior growth of grain coatings forming a barrier that prevents widespread nucleation of quartz. Grain coatings, such as chlorite, illite–chlorite, smectite, illite, and microcrystalline quartz (Bloch et al. 2002; Worden and Morad 2003; Worden et al. 2018a) are the most effective at limiting extensive quartz cementation in sandstones. Authigenic grain-coating chlorite has the tendency to form continuous layers that line the interface between detrital grains and intergranular pore space. The completeness of coverage of chlorite grain coatings is considered the principal factor dictating the effectiveness of quartz cement inhibition (Ajdukiewicz and Lander 2010; Ajdukiewicz and Larese 2012; Dowey et al. 2012). Chlorite has been the subject of many diagenetic studies where the importance of clay coatings in limiting porosity loss due to quartz cementation has been recognized (Ehrenberg 1993; Ehrenberg et al. 1998; Jahren et al. 1998; Anjos et al. 2003; Berger et al. 2009; Dutton et al. 2018; Stricker and Jones 2018).

The development of authigenic chlorite coatings during burial is dependent on chlorite precursor clay minerals, such as 7 Å clays (Ehrenberg 1993), trioctahedral smectites (McKinley et al. 2003), swelling chlorites (Humphreys et al. 1989), and kaolinite-series minerals (Moraes and De Ros 1992). Berthierine, the precursor mineral present in the samples used here, is an aluminous, Fe^{2+}-rich, 1:1 clay belonging to the kaolinite-serpentine series, often present in marginal marine sediments such as deltaic and estuarine deposits and Fe-rich sedimentary rocks (Bhattacharyya 1983; Hornibrook and Longstaffe 1996; Morad et al. 2010). Berthierine occurs as small lath-shaped grain coatings (fringes or tangentially arranged), crystals, as pellets, ooids, and void fillings (Worden and Morad 2003). Apart from clay precursors, the destabilization of eodiagenetic ferroan carbonates, such as siderite, can also produce authigenic chlorite at temperatures > 120 °C (Curtis et al. 1985).

63 The role of high temperatures (> 100 °C) in controlling authigenic chlorite coatings on detrital
64 quartz grains has been determined experimentally, with increases in individual chlorite crystal size
65 and thickness (c-axis) observed from 90 to 220 °C (Hillier 1994), and more efficient prevention of
66 quartz growth at temperatures above 115°C (Ajdukiewicz and Larese 2012). Hydrothermal
67 experiments replicating burial diagenesis qualitatively showed that thin, discontinuous, poorly
68 crystalline berthierine coatings will start to recrystallize to chamosite at about 70 °C (Aagaard et al.
69 2000). An interstratification phase occurring between 70 and 160 °C (Jahren and Aagaard 1989), and
70 the conversion is thought to be complete above 160 °C (Iijima and Matsumoto 1982). Ajdukiewicz and
71 Larese (2012) have shown that the effectiveness of clay coatings at preserving porosity depends on
72 temperature and the continuity of the coating. Grain-coating clay minerals can form on clean quartz
73 and feldspar surfaces at 100 and 150 °C, given sufficient supersaturation and time (Haile et al. 2015).

74 In this study, a multi-method approach comprising a series of temperature-controlled
75 hydrothermal reactor experiments on sandstone samples from the Lower Jurassic Cook Formation of
76 the Oseberg Field, Norway (30/6-17R), were carried out. An artificial solution and silica granules were
77 used to maintain silica-saturated conditions during each experimental run. Mineralogical evaluation,
78 using X-ray diffraction (XRD), scanning electron microscopy (SEM) and energy-dispersive X-ray
79 spectroscopy (SEM-EDS), and automated quantitative mineralogy (AQM), has been undertaken to
80 simulate and quantitatively assess berthierine-to-chlorite transformation, grain-coating chlorite
81 authigenesis, cementation, and diagenesis of the sandstone samples. The experimental results
82 complement previous studies on chlorite synthesis (Aagaard et al. 2000) and provide important
83 insights into the role played by precursor clays, temperature, and Fe-rich minerals, such as siderite,
84 upon chloritization processes, decline of quartz precipitation, and subsequent preservation of
85 reservoir quality.

MATERIALS AND METHODS

Sampling

Naturally occurring sandstone samples were obtained from core material from the Lower Jurassic Cook Formation of the Oseberg Field (Norway, Well 30/6-17R). The Cook Formation lies stratigraphically in the Dunlin Group (Pliensbachian – Toarcian) and is extensively distributed in northern North Sea. Polished blocks, rock chips, and core plugs (4 mm diameter and length varying between 5 mm and 9 mm) were taken from a prograding subtidal sand body (Livbjerg and Mjøs 1989) at a depth of 7988.18 ft. (2434.8 m), selected for the high content of berthierine and siderite.

Hydrothermal Reactor Experiments

Hydrothermal reactor experiments were carried out in a Parker Autoclave Engineers 500 ml cylindrical 316 stainless steel pressure vessel with an all-metal seal configuration operating at temperatures up to 350 °C. The vessel was heated by a ceramic band heater and, during the experiments, temperature was controlled within ± 0.5 °C through a Eurotherm© PID temperature controller. Six core plugs were subjected to hydrothermal treatment at specific temperature steps under strictly closed conditions (Table 1). For all the experimental runs, silica gel granules and an aqueous solution of 0.1 M Na_2CO_3 (reagent grade) dissolved in high-purity water (Milli-Q) were used as a source of silica and pore fluid, respectively. The experimental setup is depicted in Figure 1A.

In each experiment, five grams of silica gel and one core sample were enclosed in two different 50 µm stainless steel meshes. The meshes were then attached to the bottom of the sample holder (Fig. 1B), using stainless-steel wire, and the sample assembly was lowered into the pressure vessel. The vessel was gradually filled with 300 ml of 0.1 M Na_2CO_3 solution (giving 200 ml headspace at room temperature), sealed and heated to the experimental temperature at 2.5 °C per minute. All samples were held at the desired experimental temperature for 72 hours before the heater was switched off.

Once cooled to room temperature, the vessel was removed from the reactor, and the sample was removed and air-dried.

Natural diagenetic conditions cannot be fully reproduced in the laboratory due to the short experimental time compared to a geological timeframe and the simplification and uncertainties associated with the chosen aqueous chemistry. The experimental conditions used are chosen based on the following assumptions:

1. The experiments were conducted under zero-flow conditions mimicking a closed-system geological model. Grain-coating chlorites are likely to develop from closed-system diagenesis at the bed scale (Worden et al. 2020).

2. The artificial solution was selected so as to be nonreactive (e.g., Fe-free chemical composition) with the Fe-rich minerals and to provide CO_2 pressures of 0.2 -1 bar, typical for sedimentary systems in the North Sea (Aagaard and Egeberg 1998). Additionally, chlorite is preferentially stable under alkaline solutions (White et al. 1942).

3. Quartz dissolution is evident in many alkaline diagenetic environments (Pichat et al. 2016; Li et al. 2020). Experimental studies on quartz dissolution indicate that dissolution rates increase as the pH increases into the alkaline region (Knauss and Wolery 1988; Crundwell 2017). Additionally, the use of a 0.1 M Na_2CO_3 solution coupled with a source of silica can generate strong quartz-cementing conditions as shown by previous hydrothermal experiments investigating cement growth-limitation mechanisms (Ajdukiewicz and Larese 2012). The silica-saturated solution promotes the precipitation of quartz cement; simulating the mechanical compaction that would drive quartz cementation even when compaction cannot be performed during the experiments.

4. Prior research has shown that the applied experimental duration and temperatures are adequate to stimulate growth of clay coatings and quartz cement (Small et al. 1992;

Aagaard et al. 2000; Ajdukiewicz and Larese 2012). The initial temperature of 100 °C was selected to exceed the commonly accepted threshold of 80 °C for quartz cementation (Walderhaug et al. 2000; Lander et al. 2008) and the threshold of 60 °C proposed for berthierine-to-chlorite transformation (Ehrenberg 1993; Worden and Morad 2003).

Analytical Techniques

Sample Mineralogy.---The clay mineralogy of the initial natural sample was determined by X-ray powder diffraction (XRD). Bulk rock samples were de-oiled, disaggregated, and powdered to a mean particle diameter of 5-10 μm, and the mineralogy was analyzed using a Philips PW1730 Generator (copper anode at 40 kV, 40 mA), a PW1050 Goniometer with graphite monochromator, and a PW1170 automatic sample changer. The bulk mineralogy analysis was performed at 2θ (theta) angles = 4.5˚ - 75˚ (step size of 0.06˚/s). The clay fraction (< 2 μm fraction) was separated from the bulk rock using ultrasound and centrifugation. Analysis of the clay fraction analysis allowed the quantification of the clay mineral components. A 25 ml aliquot of the clay suspension was evaporated to dryness at 80 °C, and the total weight was determined. The samples were analyzed as an untreated clay, after saturation with ethylene glycol vapor overnight and heated at 380 ˚C for 2 hours and 550 ˚C for 1 hour. The samples were then analyzed at 2θ = 3˚ - 35˚ (step size of 0.05˚ per second). The untreated clays were also analyzed at 2θ = 24˚ - 27˚ (step size of 0.2˚/2 s) to further define kaolinite and chlorite peaks. Identification of the clay-mineral assemblages was performed by overlaying the diffractograms from the four clay treatments. Moreover, as chlorite and berthierine are not readily discriminated, reflections at higher diffraction angles (e.g., d_{060}) were measured.

An untreated and six hydrothermally treated cores were encapsulated in resin and a circular cross section exposed using diamond polish for SEM examination. The polished blocks were carbon-coated and backscatter (BSE) SEM imaging was carried out on a Hitachi SU-70 FEG SEM scanning electron microscope with an energy-dispersive detector (EDS) (GJ Russell Microscopy Facility, Durham University), at acceleration voltages of 20 kV and measured beam current of 0.6 nA. SEM-EDS was

used for rapid elemental identification on randomly selected areas in each polished block sample. In addition, secondary electron (SE) SEM imaging was conducted on an untreated rock chip and a small fraction of rock that was carefully detached from the core plug was subjected to hydrothermal treatment at 250 °C before encapsulation. The gold-coated samples were analyzed at an acceleration voltage of 5 kV with a beam current of 1 nA.

AQM was also performed on the polished blocks to quantify the mineralogy and characterize the petrographic relations at each temperature step. A Zeiss Gemini SUPRA 40VP field emission scanning electron microscope coupled with a Bruker XFlash® 60 EDS detector and Mineralogic software suite were used for the EDS spectra acquisition and digital analysis, respectively. Images were collected using a high-resolution raster, with step size of 3.5 µm at a 255x magnification and a 20 kV acceleration voltage. Dwell time was adjusted to capture approximately 20,000 counts per pixel. After differentiating the mineral phases from the epoxy resin by thresholding the gray BSE image before EDS analysis, a mineral-classification library tailored to this research was developed using the initial XRD, SEM-BSE and SEM-EDS analyses. AQM compared the EDS spectra of each point to the library, assigning a specific mineral to each point and producing a mineralogical map.

Coating Thickness, Grain-Coat Coverage and Porosity Quantification.---ImageJ was used to measure coating thickness from the BSE images at 50 points per sample (± 0.05 µm). The measured thicknesses were binned into four classes: 1) 1-3 µm; 2) 3-5 µm; 3) 5-7 µm, and 4) 5-9 µm, to evaluate any changes in distribution between the different hydrothermal treatments. Grain-coating coverage was quantified using Petrog (Wooldridge et al. 2019), with the percentage perimeter of a grain-coated with clay calculated by measuring its total perimeter and the length covered by attached clay for 50 grains for each of the different hydrothermal treatments. The standard error of the analysis of each sample was ± 2%.

Before the preparation of the polished blocks, each core was imaged using X-ray microtomography to accurately derive the volume of each. Scanning was performed on a Zeiss Xradia VersaXRM 410

scanner (Durham University) operating at 80 kV (no beam filtration). All samples were imaged with a spatial resolution of 3.8 µm/voxel (3D equivalent of a pixel). Subsequently, each core was subjected to helium pycnometry analysis on a Micromeritics AccuPyc II 1340 pycnometer and, by using the micro-CT-derived volume, numerical porosity data were generated. In addition, 2D porosity was extracted by the SEM-BSE image of each polished block using the digital image-analysis technique, jPOR (Grove and Jerram 2011).

RESULTS

Mineralogical Evaluation of the Cook Formation Before the Hydrothermal Experiments

The composition of the Cook Formation comprises medium- to fine-grained, moderately sorted, angular to subangular grains. EDS elemental mapping illustrates the increased iron content in the sample (Fig. 2). Bulk X-ray diffraction analysis suggests the dominance of quartz as a primary mineral, with kaolinite and berthierine being the clay minerals, and siderite the main carbonate mineral identified. The clay-fraction analysis proves that berthierine is the main Fe-rich clay in the sample. Chlorite occurs in traces only (Table 2). Figure 3A shows the overlaid diffractograms after the various chemical and heat treatments. Kaolinite has its 001 peak at 12.39° 2θ, chlorite has its 002 peak at 12.29-12.55° 2θ, and berthierine has the 001 peak at 12.52° 2θ. The 002 peak of kaolinite is at 24.9° 2θ, the 004 peak of chlorite is at 25.1-25.2° 2θ, and the 002 peak of berthierine is at 25.2° 2θ. The presence of a peak at 12.40° 2θ after the heat treatment at 550 °C for one hour is proof of the presence of kaolinite. The presence of trace of chlorite is shown by the peak at 6.3 °2θ after the heat treatment at 550 °C. The presence of berthierine is indicated by the reduction of intensity of the peak at 25.2° 2θ after the heat treatment at 380 °C for two hours. Additionally, the d_{060} reflection value for kaolinite is about 1.490 Å (62.31° 2θ), for chlorites is about 1.538-1.549 Å (60.15-59.69° 2θ) and for berthierine is about 1.555 Å (59.44° 2θ) (Fig. 3B). No other clay mineral has its d_{060} peak in this position (Bailey 1980).

Three forms of berthierine were distinguished based on their morphological characteristics. 1) Thick concentrically laminated ooidal coatings with thickness ranging from 10 to 50 µm (Fig. 4A). 2) Thin, patchy and discontinuous grain coatings covering detrital grains with an average thickness of 3.6 µm (Fig. 4B). The thickest expressions have been preferentially observed in grain indentions. 3) Pore-filling material (Fig. 4D).

Quartz, orthoclase, albite, and Ti-rich grains have been observed at the center of the ooidal structures acting as nucleus grains. In this case, berthierine identified at the outer cortex of the ooid shows a fibrous texture. In contrast, the patchy berthierine coats comprise a network of poorly developed, flake-shaped crystals (Fig. 5B) lying subparallel to the surface of the host grains. Edged surfaces and cavities appear to favor the presence of berthierine. Quartz-overgrowth development and siderite cement are associated with these coatings (Fig. 5A). Finely crystalline (< 50 µm) siderite occurs on the rims of framework grains postdating berthierine precipitates (Fig. 4C). Crystals lying directly on host grain surfaces are also common. Crystal habit includes lozenge-shaped isolated crystals (Fig. 5D), and aggregates of those. Berthierine is associated with kaolinite (Fig. 5C), the main pore-filling material identified. Kaolins present face-to-face stacks of thin, irregular, pseudohexagonal plates with ragged edges. Microporosity is visible in the pore filling.

The applied automated mineralogy technique allowed collection of chemical data across each sample. The EDS spectra of each analyzed point were automatically compared to the newly developed mineral classification that includes the pre-defined chemical compositions of each mineral observed throughout the experimental steps. The sandstone can be classified as subarkosic, comprising, by weight, approximately 54% quartz. Orthoclase is the most common alkali feldspar (~ 11%) and albite the most common plagioclase (~ 5%). In agreement with the XRD results, kaolinite (~ 9%) and berthierine (~ 6%) are the most abundant clay minerals, while siderite (~ 8%) the most common carbonate cement. This technique also identified small amounts of chlorite (< 2%).

SEM-EDS and AQM analysis was performed on core samples, taken from locations adjacent to the ones used for the hydrothermal experiments, to evaluate the significance of the compositional variability of the pre-reaction material. The analysis was performed both perpendicular and longitudinal to the long axis of the cores and suggests a consistent mineral distribution. For the modal mineralogy and relevant elemental composition of the untreated Cook Formation please refer to the supplementary material.

Post-Experiment Mineralogical Evaluation

Berthierine-to-Chlorite Transformation.---The focus of the AQM analysis was to identify, separate, and quantify berthierine and chlorite phases at each experimental step. Berthierine and chlorite have similar chemical compositions, hence potential minor differences in elemental concentrations are required for the successful distinction between the two. The range of the elemental concentration for the identification of berthierine was determined by collecting EDS spectra from the ooidal and grain-coating structures in the initial sample, where berthierine was present with certainty. Similarly, the chemical signature of chlorite was determined by targeting the neoformed chlorite grain coatings in the samples from the higher-temperature experiments. The two chemical compositions showed a subtle difference in the aluminum concentration, which in berthierine and chlorite was ~ 17 wt.% and ~ 5 wt.%, respectively. Previous studies on berthierine formation and chlorite authigenesis also confirm that berthierine is aluminum-rich (Iijima and Matsumoto 1982; Curtis et al. 1984).

The produced mineralogy maps illustrate the high berthierine content at 100 °C (Fig. 6A) and the elevated chlorite content at 250 °C (Fig. 6C). There is an increasing contact association between berthierine and chlorite with increasing temperature while the initial strong association of berthierine with pore space is diminishing (Fig. 6B). Chlorite shows significant contact with quartz and siderite in each temperature step (Fig. 6D). The declining trend regarding quartz is credited to the increase in chlorite content, therefore associated with more and different minerals.

Occurrence and Morphology of Authigenic Chlorite.---The following petrographic types of authigenic chlorite were observed: 1) grain coatings (Fig. 7A, B), 2) rosette-like clusters on the chloritized surfaces expanding into the pore space (Fig. 7C), and 3) cabbage-head chlorites affixing at the platelets of the grain-coating chlorites (Fig. 7D). The grain coatings form independently of size and shape of the substrate grains. They consist of euhedral, pseudohexagonal crystals oriented perpendicular to subperpendicular to the grain surfaces with a face-to-edge and face-to-face foliaceous pattern. The less volumetrically significant chlorite rosettes are composed of euhedral platelets in a divergent arrangement. Cabbage-head chlorite aggregates are mainly observed affixing at the surface of well-developed chlorite surfaces. Small amounts are formed directly on the substrate grain surfaces.

Siderite Occurrence and Chlorite Authigenesis.---With increasing temperature, siderite crystals display zonation patterns in terms of iron, calcium, and magnesium contents (Fig. 8A). From core to rim the calcium content is decreasing. A magnesium-enriched zone is observed in the middle part of the crystals. Central dissolution voids, containing increased calcium and magnesium concentrations, were mainly observed at temperatures higher than 200 °C (Fig. 8B). SEM imaging illustrates the partial or complete engulfment of siderite by authigenic chlorite crystals (Fig. 8C, E) and the presence of calcite crystals beside siderite dissolution voids which most likely acted as seeds for siderite development (Fig. 8D). Chlorite-coating precipitation was enhanced on host grain surfaces directly next to the dissolving siderite crystals (Fig. 8E). Therefore, the thickest authigenic chlorite coatings were observed next to siderite crystals whose initial rhombic shape was progressively deformed to rounded crystal faces.

Quartz Cement and Other Diagenetic Alterations.---The abundance of quartz in each sample, pre- and post-experiment, remained constant at ~ 50%. Replacement of kaolinite by dickite was recognized by the gradual coarsening and morphological evolution of the kaolinite crystals. Dickite presents a euhedral blocky habit as opposed to the booklet morphology of the initial pseudohexagonal kaolinite

crystals. Based on SEM imaging, minor formation of zeolite minerals, such as natrolite presenting a prismatic habit and analcime showing a trapezohedron form, was observed at Experiments 5 and 6.

Quantification of Berthierine-to-Chlorite Transformation, Clay-Coat Characteristics, and Porosity Evolution

The AQM method displays a progressive decrease of berthierine and concurrent increase of chlorite content (Fig. 9A). The temperature range of berthierine-to-chlorite transformation is constrained between 100 °C and 175 °C, with approximately 150 °C being the critical temperature where chlorite overcomes berthierine content. The results from Experiment 6 showed that, by weight, berthierine decreased to ~ 1% while chlorite increased to ~ 14%.

The dataset from the quantitative, Petrog-based, analysis revealed an increasing trend of the coating coverage with increasing temperature. The temperatures of 150 °C and 200 °C exhibit the main increment zone with average values of ~ 28% and ~ 47%, respectively (Fig. 9B). No significant increase occurred beyond that point. However, surface area covered by clay coats was observed on every grain. Pre-experimental clay-free surfaces coated by siderite crystals (Fig. 10A) present extensive coverage after the hydrothermal runs at the highest temperatures (Fig 10C).

A frequency histogram illustrating the distribution of the thickness of the clay coatings, in four categories, with increasing temperature is depicted in Figure 9C. 74% of the measurements belonging to Class 1 derive from samples hydrothermally treated up to 150 °C. Group 2 presents a uniform distribution between each temperature step. A significant increase in the coating thickness is observed in temperatures greater than 175 °C. On average 33% of the measurements belonging to Classes 3 and 4 derive from Experiment 6.

Results of helium pycnometry showed a porosity decrease from an initial value of ~ 28% to ~ 23% at 250 °C. The main porosity reduction phase takes place between 150 °C and 175 °C followed by a maintenance phase. 2D porosity measurements reveal a similar trend; however, there is a 6.5% discrepancy between the helium and jPOR techniques (Fig. 9D). Reduction of primary porosity is

306 mainly ascribed to the alteration of kaolinite to dickite (Fig. 10B, D). Visibility of microporosity in the
307 pore filling is progressively decreasing from 175 °C onwards. Secondary porosity is generated through
308 the dissolution of albite and siderite grains.

309 **DISCUSSION**

310 The present-day depth and temperature of the Cook Formation is approximately 2400 m and 90
311 °C, respectively. Therefore, assuming that the borderline between the eodiagenetic and
312 mesodiagenetic realm is at about 2000 m depth and 70-90 °C temperature (Worden and Burley 2003),
313 the Cook Formation is an ideal candidate for developing a better understanding about mineral
314 diagenetic alterations occurring during the transition from eodiagenesis to mesodiagenesis.

315 Several, mainly isochemical, reactions have been reported as responsible for chlorite authigenesis
316 in deeply buried sandstones (Curtis et al. 1985; Smith and Ehrenberg 1989; Worden and Morad 2003;
317 Worden et al. 2018b). The main detrital and early diagenetic Fe-rich minerals involved in these
318 reactions include detrital chlorite and biotite, berthierine, trioctahedral smectite, siderite, ankerite,
319 ilmenite, and other Fe-rich heavy minerals (Worden et al. 2020). In this paper, an experimental
320 approach has been taken to investigate berthierine to chlorite transformation and subsequent
321 association of the generated authigenic chlorite with reservoir-quality evolution (Fig. 11). The
322 experimental results quantitatively identify that berthierine can be a precursor for chlorite
323 precipitation in sandstones, and in the presence of siderite will produce robust clay coatings on clean
324 substrate surfaces or where berthierine and siderite precursors pre-exist.

325 ***Initial Berthierine and Siderite***

326 Although various genetic pathways for the precipitation of berthierine have been proposed
327 (Bhattacharyya 1983; Van Houten and Purucker 1984; Harder 1989; Mu et al. 2015), an abundant
328 supply of Fe and reducing conditions are essential for its crystallization (Curtis and Spears 1968; Curtis
329 1985). Based on the proposed depositional environment of the sandstone used, berthierine is most
330 likely the product of early diagenesis. The Cook sandstone was interpreted as a prograding sandflat

formed in a tide-influenced marginal marine setting (Livbjerg and Mjøs 1989). Depositional settings in the vicinity of river mouths favor the development of berthierine (Ehrenberg 1993; Worden and Morad 2003; Morad et al. 2010) due to brackish pore-water compositions, which have low concentrations of dissolved sulfate ions, abundant supply of iron-bearing particles via river waters (Bailey 1988; Odin 1988; Odin 1990), and high sedimentation rates promoting anoxic conditions. The absence of pyrite in the samples suggests negligible bacterial sulfate reduction processes such that sufficient concentrations of Fe^{2+} will be present enabling berthierine precipitation.

The morphology of the siderite cement and the textural evidence of siderite postdating berthierine (Figs. 4C, 5D) indicate precipitation at a later diagenetic stage. Early diagenetic siderite mostly develops in the form of nodules or more pervasive cement (Curtis et al. 1986) whereas the lozenge-shaped crystals fringing detrital grains observed in the samples are common precipitates in early mesodiagenesis. Siderites with similar crystal habit have been found synchronous with quartz overgrowths (Karim et al. 2010).

Authigenic Grain Coating Chlorite

Berthierine-to-Chlorite Transition.---The conversion of berthierine to chlorite has been proposed to occur at temperatures greater than 60 °C (Jahren and Aagaard 1989; Aagaard et al. 2000; Worden and Morad 2003). Mineral reactions take place through different mechanisms which have different activation energies, therefore affected by different temperatures (Lasaga 1998). Based on our observations, chloritization of berthierine is the product of a mixture of the solid-state transformation (SST) and dissolution-precipitation (DC) mechanisms.

Solid-state transformation (SST) can explain the chloritization of berthierine up to an experimental temperature of ~ 150 °C. SST is less energetically demanding than DC, as it requires less disruption of chemical bonds, and thus is favorable in lower-energy settings. SST has been proposed by several authors as the dominant mechanism responsible for the progressive replacement of 7Å-layered minerals by 14Å-layered minerals (Banfield and Bailey 1996; Ryan and Reynolds 1996; Xu and Veblen

1996). According to SST, phyllosilicate reactions are relatively volume conservative retaining the crystal habit and leading to similar shape and size between the parental and daughter minerals. AQM revealed an increase in chlorite and a concomitant decrease in berthierine content; however, the sum of the volume of the two minerals, up to 150 °C, remained constant. SEM examination did not show any evidence for dissolution features and no change in the average clay-coating thickness and coverage was observed.

An increase in temperature is one of the factors that has been considered to raise the possibility of DC (Altaner and Ylagan 1997). DC requires large morphological changes between the initial and final clay mineral (Cuadros 2012). In natural systems, the recrystallization of low-temperature, berthierine-derived, chlorites to the higher-temperature chlorites is efficient at temperatures near 200 °C (Walker 1993). This process involves an increase in crystal size and structural changes such as polytype transformation and disappearance of the berthierine-chlorite interstratifications (Hillier 1994). The significant increase in chlorite volume (Fig. 9A), the new rosette and cabbage head chlorite precipitates (Fig. 7), and the increase in coat thickness (Fig. 9C) and coverage (Fig. 9B) at temperatures between 175 °C and 250 °C indicate a transition from the SST to the DC mechanism. DC also requires dissolution of entire mineral particles with their dissolved species passing into the bulk of the solution to provide the necessary reactive elements for chlorite authigenesis. Al and Fe were sourced principally from the albite and siderite decomposition, respectively, which occurred with increasing temperature.

Assessment of the hydrothermal reactor experiments provides valuable quantitative and qualitative data on the transformation of berthierine to chlorite as a function of temperature. The incorporation of fluid chemistry offers great potential for chlorite prediction at the field and reservoir scales.

Role of Siderite and Neoformation of Authigenic Chlorite Coatings.---The high contact association of siderite with chlorite suggests the interdependence between the two minerals (Fig. 6D).

Chloritization of siderite proceeds solely through the DC mechanism. Siderite dissolution promotes chlorite authigenesis as evidenced by the thick chlorite coatings observed adjacent to decomposing siderite crystals (Fig 8E) and by the complete engulfment of the dissolving crystals by authigenic chlorite (Fig. 8F).

Iijima and Matsumato (1982) have proposed the dissolution of siderite as a source of Fe for chlorite. They demonstrated the replacement of siderite by berthierine and subsequent berthierine-to-chlorite transformation in Paleogene and upper Triassic coal-measure formations in Japan. Chlorite neoformation as a direct precipitate from solution, directly on clean, mainly quartz, surfaces (Fig. 10C), contributes to the major increase in the volume of chlorite at 250 °C. Previous hydrothermal experiments have also demonstrated that authigenic chlorites can be direct precipitates and do not necessarily require pre-existing precursors (Small et al. 1992; Haile et al. 2015).

Effect of Grain Coats on Quartz Cementation and Porosity Evolution

The present porosity (~ 28%) of the Cook Formation is solely accredited to mechanical compaction processes and is in accord with porosity values of siliciclastic reservoirs that have not yet entered the chemical compaction phase (Houseknecht 1987; Paxton et al. 2002; Taylor et al. 2010).

Minor amounts of clay, as little as 1–2% of the rock volume, have the ability to coat large surface areas of sandstone grains and affect reservoir quality positively (Bloch et al. 2002). The authigenic chlorite coatings produced in our experiments increase in continuity and thickness, thus preserving porosity at an average value of ~ 23% at temperatures between 175 °C and 250 °C. Grain coverage, from both chlorite and siderite crystals, insulates the grains and decreases the surface area available for quartz precipitation. Moreover, the enrichment of the initial Si-supersaturated solution with Al and Fe compounds strengthens chlorite authigenesis at the expense of quartz cement. The ~ 5% reduction of porosity is attributed mainly to dickite authigenesis occluding primary pores. Secondary porosity through albite and siderite dissolution contributes to the maintenance of overall porosity.

405 The optimum chlorite coat volume and thickness that will not result in the deterioration of the
406 reservoir quality of a given reservoir is variable, and depends mainly on pore and pore-throat size.
407 Pittman et al. (1992) suggested an optimum volume ranging between 5 and 13% for the Tuscaloosa
408 Formation and between 4% and 7% for the Berea Sandstone. A coating thickness between 5 µm and
409 10 µm has been documented in several studies as beneficial for preservation of reservoir quality
410 (Anjos et al. 2003; Sun et al. 2014). In agreement with these observations, the volume and thickness
411 of the synthesized chlorite coatings have not exceeded 14% and 10 µm, respectively. Quartz
412 cementation is effectively retarded without occluding primary pores.

413 ***Relevance of Experiments to Subsurface Analogs***

414 Although the experimental conditions were modeled as closely as possible to reservoir conditions,
415 there are some differences. The short duration of the experiments and the simplified fluid chemistry
416 are key differences but they are partially compensated for by the elevated temperatures used for the
417 experiments in this study. Furthermore, all the experiments started with an excess supply of silica to
418 instigate quartz cementation. In natural settings, such conditions occur over prolonged periods of
419 geological time, with silica and other reactants being derived from various sources.

420 In the Knarr (Well 34/3-1S) and Veslefrikk (Well 30/3-4) Fields, offshore Norway, the Cook Formation
421 reservoir is located at depths of ~ 3700 m and ~ 3000 m, respectively. The corresponding temperature
422 is ~135 °C, and the presence of partial or complete chlorite coatings is significant, allowing the
423 preservation of excellent reservoir quality (Hasnain and Jahren 2017; Skarpeid et al. 2017). Given the
424 present-day depth (2400 m), temperature (90 °C), and absence of chlorites in the pre-experiment
425 samples, one can hypothesize that the conversion of berthierine takes place between 90 °C and 135
426 °C. The study by Jahren and Aagaard (1989) on samples from multiple Jurassic clastic reservoirs
427 offshore Norway suggests that continuous recrystallization of berthierine to chlorite occurs between
428 70 °C and 160 °C. At higher temperatures, berthierine is rendered unstable relative to chlorite (Iijima
429 and Matsumoto 1982). The experimental results have produced observations comparable to the

aforementioned natural systems showing that the main temperature window of berthierine to chlorite conversion lies between 100 °C and 175 °C with a noticeable stepwise change at ~ 150 °C, where chlorite becomes the dominant phase compared to the precursor berthierine clay. Likewise, the produced chlorite coatings significantly inhibit quartz overgrowth development.

Further experiments remain to be performed using a volumetrically low fluid-to-rock ratio in a hydrothermal setup that allows fluid sampling at experimental conditions. This, to study the role of fluid chemistry, representative of the microenvironment of clay precipitation, of the core material both pre- and post-reaction, and develop a more comprehensive understanding of the chemical and reaction parameters for authigenic chlorite formation.

Implications for Prediction of Reservoir Quality

The ability to predict the presence of grain-coating chlorite, and any other reservoir quality-influencing authigenic mineral, would lead to better-informed decisions during oil and gas exploration and for geothermal exploration where predictive models of reservoir properties are critical. Chlorite has been the subject of many diagenetic studies; however, no proven method of predicting chlorite coats in data-poor frontier settings exists. In more mature settings where core data are available, the probability of chlorite coatings can be assessed using sedimentological and petrographic data sets (Berger et al. 2009; Sun et al. 2014; Stricker et al. 2016; Dutton et al. 2018; Stricker and Jones 2018). Studies of the distribution of precursor clay coatings and chlorite in modern sedimentary environments have revealed that it is imperative to define specific sub-environments of deposition to fully understand and predict chlorite grain coats in ancient and deeply buried sandstones (Wooldridge et al. 2017; Griffiths et al. 2018; Griffiths et al. 2019a; Griffiths et al. 2019b; Virolle et al. 2019; Virolle et al. 2020). Temperature plays a key role in the rate of authigenic-chlorite precipitation in sandstones. The experimental approach applied in this study has clearly recognized that with the correct geochemical components and progressive temperature increase within a sandstone body, then chlorite coatings develop in preference to quartz cement. The quantitative data, assessing the

thermally driven chlorite-coating authigenesis from precursor minerals, can be used to improve predictability of reservoir quality modeling in high-temperature (> 150 °C), deeply buried reservoir sandstones.

CONCLUSIONS

1. Hydrothermal experiments simulating burial diagenesis, using naturally occurring sandstone samples, selected for their initial content of berthierine and siderite, and an artificial silica-supersaturated solution, were undertaken at specific temperature steps and constant duration to assess the impact of chlorite authigenesis on reservoir quality of sandstones. Quantitative datasets regarding i) the volume of berthierine and chlorite, ii) the clay-coating thickness and coverage and, iii) porosity were produced at each temperature step.

2. The hydrothermal-reactor experiments have identified berthierine as precursor for chlorite in high-temperature environments. In addition, the experiments reveal the significant role of siderite to allow continued authigenesis of chlorite as grain coatings. Chlorite is formed from berthierine transformation, replacement of siderite and neoformation on precursor-free substrate surfaces. Dissolution of albite and siderite provided the Al and Fe ions, important for chlorite authigenesis.

3. Chlorite authigenesis initiates with solid-state transformation at low experimental temperatures (100 °C) transitioning to dissolution crystallization at the higher-temperature spectrum. The threshold temperature for this transition is ~ 150 °C. Future long-duration experiments using various fluid compositions are needed to further develop and confirm these initial findings.

4. The hydrothermally synthesized chlorite coatings are morphologically akin to naturally occurring chlorite coatings. A significant increase in clay-coating thickness (form an average value of 3.8 µm at 150 °C to 5.4 µm at 250 °C) and clay coverage (from ~ 28% at 150 °C to ~ 50% at 250 °C) resulted in porosity preservation through offering fewer nucleation sites for quartz to precipitate. Dickitization of kaolinite is the dominant process reducing primary porosity. Secondary

intracrystalline porosity contributing to the overall porosity maintenance was generated by the dissolution of albite and siderite crystals.

ACKNOWLEDGMENTS

Durham University is thanked by Dimitrios for sponsoring this project through a Durham Doctoral Studentship. We would also like to acknowledge support from BP for access to the SEM facilities and extensive advice offered. Phil Dyer (Durham University) and Jackie Kendrick (University of Liverpool) are thanked for help and assistance with the autoclave experiments and helium-porosity determination, respectively.

REFERENCES

AAGAARD, P., AND EGEBERG, P.K., 1998, Formation waters and diagenetic modifications: general trends exhibited by oil fields from the Norwegian shelf - A model for formation waters in oil prone subsiding basins, *in* Arehart, G.B., and Hulston, J.R., eds., Water-Rock Interaction: Proceedings of the 9th International Symposium, Balkema, p. 281-286.

AAGAARD, P., JAHREN, J.S., HARSTAD, A.O., NILSEN, O., AND RAMM, M., 2000, Formation of grain-coating chlorite in sandstones. Laboratory synthesized vs. natural occurrences: Clay Minerals, v. 35, p. 261-269.

AJDUKIEWICZ, J.M., AND LANDER, R.H., 2010, Sandstone reservoir quality prediction: the state of the art: American Association of Petroleum Geologists, Bulletin, v. 94, p. 1083-1091.

AJDUKIEWICZ, J.M., AND LARESE, R.E., 2012, How clay grain coats inhibit quartz cement and preserve porosity in deeply buried sandstones: observations and experiments: American Association of Petroleum Geologists, Bulletin, v. 96, p. 2091-2119.

ALTANER, S.P., AND YLAGAN, R.F., 1997, Comparison of structural models of mixed-layer illite/smectite and reaction mechanisms of smectite illitization: Clays and Clay Minerals, v. 45, p. 517-533.

ANJOS, S.M.C., DE ROS, L.F., AND SILVA, C.M.A., 2003, Chlorite authigenesis and porosity preservation in the Upper Cretaceous marine sandstones of the Santos Basin, offshore eastern Brazil, *in*

Worden, R.H., and Morad, S., eds., Clay Mineral Cements in Sandstones: International Association of Sedimentologists, Special Publication 34, p. 291-316.

BAILEY, S., 1980, Structures of layer silicates, *in* Brindley, G.W., and Brown, G., eds., Crystal Structures of Clay Minerals and Their X-Ray Identification: Mineralogical Society, Monograph 5, p. 1-123.

BAILEY, S.W., 1988, Odinite, a new dioctahedral-trioctahedral Fe^{3+}-rich 1:1 clay mineral: Clay Minerals, v. 23, p. 237-247.

BANFIELD, J.F., AND BAILEY, S.W., 1996, Formation of regularly interstratified serpentine-chlorite minerals by tetrahedral inversion in long-period serpentine polytypes: American Mineralogist, v. 81, p. 79-91.

BERGER, A., GIER, S., AND KROIS, P., 2009, Porosity-preserving chlorite cements in shallow-marine volcaniclastic sandstones: Evidence from Cretaceous sandstones of the Sawan gas field, Pakistan: American Association of Petroleum Geologists, Bulletin, v. 93, p. 595-615.

BHATTACHARYYA, D.P., 1983, Origin of berthierine in ironstones: Clays and clay minerals, v. 31, p. 173-182.

BJØRLYKKE, K., AND EGEBERG, P., 1993, Quartz cementation in sedimentary basins: American Association of Petroleum Geologists, Bulletin, v. 77, p. 1538-1548.

BLOCH, S., LANDER, H.R., AND BONNELL, L., 2002, Anomalously high porosity and permeability in deeply buried sandstone reservoirs: origin and predictability: American Association of Petroleum Geologists, Bulletin, v. 86, p. 301-328.

CRUNDWELL, F.K., 2017, On the mechanism of the dissolution of quartz and silica in aqueous solutions: American Chemical Society Omega, v. 2, p. 1116-1127.

CUADROS, J., 2012, Clay crystal-chemical adaptability and transformation mechanisms: Clay Minerals, v. 47, p. 147-164.

CURTIS, C.D., 1985, Clay mineral precipitation and transformation during burial diagenesis: Royal Society (London), Philosophical Transactions, Series A, Mathematical and Physical Sciences, v. 315, p. 91-105.

CURTIS, C.D., AND SPEARS, D.A., 1968, The formation of sedimentary iron minerals: Economic Geology, v. 63, p. 257-270.

CURTIS, C.D., IRELAND, B.J., WHITEMAN, J.A., MULVANEY, R., AND WHITTLE, C.K., 1984, Authigenic chlorites: problems with chemical analysis and structural formula calculations: Clay Minerals, v. 19, p. 471-481.

CURTIS, C.D., HUGHES, C.R., WHITEMAN, J.A., AND WHITTLE, C.K., 1985, Compositional variation within some sedimentary chlorites and some comments on their origin: Mineralogical Magazine, v. 49, p. 375-386.

CURTIS, C.D., COLEMAN, M.L., AND LOVE, L.G., 1986, Pore water evolution during sediment burial from isotopic and mineral chemistry of calcite, dolomite and siderite concretions: Geochimica et Cosmochimica Acta, v. 50, p. 2321-2334.

DOWEY, P.J., HODGSON, D.M., AND WORDEN, R.H., 2012, Pre-requisites, processes, and prediction of chlorite grain coatings in petroleum reservoirs: a review of subsurface examples: Marine and Petroleum Geology, v. 32, p. 63-75.

DUTTON, S.P., HUTTON, M.E., AMBROSE, W.A., CHILDERS, A.T., AND LOUCKS, R.G., 2018, Preservation of reservoir quality by chlorite coats in deep Tuscaloosa sandstones, Central Louisiana, U.S.A.: Gulf Coast Association of Geological Societies, v. 7, p. 46-58.

EHRENBERG, S.N., 1993, Preservation of anomalously high porosity in deeply buried sandstones by grain-coating chlorite: examples from the Norwegian continental shelf: American Association of Petroleum Geologists, Bulletin, v. 77, p. 1260-1286.

EHRENBERG, S.N., DALLAND, A., NADEAU, P.H., MEARNS, E.W., AND AMUNDSEN, E.F., 1998, Origin of chlorite enrichment and neodymium isotopic anomalies in Haltenbanken sandstones: Marine and Petroleum Geology, v. 15, p. 403-425.

GRIFFITHS, J., WORDEN, R.H., WOOLDRIDGE, L.J., UTLEY, J.E.P., AND DULLER, R.A., 2018, Detrital Clay Coats, Clay Minerals, and Pyrite: A Modern Shallow-Core Analogue For Ancient and Deeply Buried Estuarine Sandstones: Journal of Sedimentary Research, v. 88, p. 1205-1237.

556 GRIFFITHS, J., WORDEN, R.H., WOOLDRIDGE, L.J., UTLEY, J.E.P., AND DULLER, R.A., 2019a, Compositional
557 variation in modern estuarine sands: Predicting major controls on sandstone reservoir quality:
558 American Association of Petroleum Geologists, Bulletin, v. 103, p. 797-833.
559 GRIFFITHS, J., WORDEN, R.H., WOOLDRIDGE, L.J., UTLEY, J.E.P., DULLER, R.A., AND EDGE, R.L., 2019b, Estuarine
560 clay mineral distribution: Modern analogue for ancient sandstone reservoir quality prediction:
561 Sedimentology, v. 66, p. 2011-2047.
562 GROVE, C., AND JERRAM, D.A., 2011, jPOR: An ImageJ macro to quantify total optical porosity from blue-
563 stained thin sections: Computers & Geosciences, v. 37, p. 1850-1859.
564 HAILE, B.G., HELLEVANG, H., AAGAARD, P., AND JAHREN, J., 2015, Experimental nucleation and growth of
565 smectite and chlorite coatings on clean feldspar and quartz grain surfaces: Marine and
566 Petroleum Geology, v. 68, p. 664-674.
567 HARDER, H., 1989, Mineral genesis in ironstones: a model based upon laboratory experiments and
568 petrographic observations, *in* Young, T.P., and Taylor, W.E.G., eds., Phanerozoic Ironstones:
569 Geological Society of London, Special Publication 46, p. 9-18.
570 HASNAIN, S.M., AND JAHREN, J., 2017, Reservoir quality preserving processes in Lower Jurassic Cook
571 Formation of Veslefrikk area, 79th EAGE Conference and Exhibition 2017, European
572 Association of Geoscientists & Engineers, p. 1-3.
573 HILLIER, S., 1994, Pore-lining chlorites in siliciclastic reservoir sandstones: electron-microprobe, sem
574 and xrd data, and implications for their origin: Clay Minerals, v. 29, p. 665-679.
575 HORNIBROOK, E.R., AND LONGSTAFFE, F.J., 1996, Berthierine from the lower cretaceous Clearwater
576 formation, Alberta, Canada: Clays and Clay Minerals, v. 44, p. 1-21.
577 HOUSEKNECHT, D.W., 1987, Assessing the relative importance of compaction processes and
578 cementation to reduction of porosity in sandstones: American Association of Petroleum
579 Geologists, Bulletin, v. 71, p. 633-642.
580 HUMPHREYS, B., SMITH, S.A., AND STRONG, G.E., 1989, Authigenic chlorite in Late Triassic sandstones from
581 the Central Graben, North Sea: Clay Minerals, v. 24, p. 427-444.

582 IIJIMA, A., AND MATSUMOTO, R., 1982, Berthierine and chamosite in coal measures of Japan: Clays and
583 Clay Minerals, v. 30, p. 264-274.
584 JAHREN, J., AND AAGAARD, P., 1989, Compositional variations in diagenetic chlorites and illites, and
585 relationships with formation-water chemistry: Clay Minerals, v. 24, p. 157-170.
586 JAHREN, J., OLSEN, E., AND BJØRLYKKE, K., 1998, Chlorite coatings in deeply buried sandstones - examples
587 from the Norwegian shelf, *in* Arehart, G.B., and Hulston, J.R., eds., Water-Rock Interaction:
588 Proceedings of the 9th International Symposium, Balkema, p. 321-324.
589 KARIM, A., PE-PIPER, G., AND PIPER, D.J.W., 2010, Controls on diagenesis of Lower Cretaceous reservoir
590 sandstones in the western Sable Subbasin, offshore Nova Scotia: Sedimentary Geology, v. 224,
591 p. 65-83.
592 KNAUSS, K.G., AND WOLERY, T.J., 1988, The dissolution kinetics of quartz as a function of pH and time at
593 70°C: Geochimica et Cosmochimica Acta, v. 52, p. 43-53.
594 LANDER, R.H., LARESE, R.E., AND BONNELL, L.M., 2008, Toward more accurate quartz cement models: The
595 importance of euhedral versus noneuhedral growth rates: American Association of Petroleum
596 Geologists, Bulletin, v. 92, p. 1537-1563.
597 LASAGA, A.C., 1998, Kinetic Theory in the Earth Sciences: Princeton, New Jersey, Princeton University
598 Press, 811 p.
599 LI, S., TIAN, J., LIN, X., ZUO, Y., KANG, H., AND YANG, D., 2020, Effect of alkaline diagenesis on sandstone
600 reservoir quality: Insights from the Lower Cretaceous Erlian Basin, China: Energy Exploration
601 & Exploitation, v. 38, p. 434-453.
602 LIVBJERG, F., AND MJØS, R., 1989, The Cook Formation, an offshore sand ridge in the Oseberg area,
603 northern North Sea, *in* Collinson, J.D., ed., Correlation in Hydrocarbon Exploration: Norwegian
604 Petroleum Society, Graham and Trotman, p. 299-312.
605 MCBRIDE, E.F., 1989, Quartz cement in sandstones: a review: Earth-Science Reviews, v. 26, p. 69-112.
606 MCKINLEY, J.M., WORDEN, R.H., AND RUFFELL, A.H., 2003, Smectite in sandstones: a review of the controls
607 on occurrence and behavior during diagenesis, *in* Worden, R.H., and Morad, S., eds., Clay

608 MIneral Cements in Sandstones: International Association of Sedimentologists, Special
609 Publication 34, p. 109-128.
610 MORAD, S., AL-RAMADAN, K., KETZER, J.M., AND DE ROS, L.F., 2010, The impact of diagenesis on the
611 heterogeneity of sandstone reservoirs: a review of the role of depositional facies and
612 sequence stratigraphy: American Association of Petroleum Geologists, Bulletin, v. 94, p. 1267-
613 1309.
614 MORAES, M.A., AND DE ROS, L.F., 1992, Depositional infiltrated and authigenic clays in fluvial sandstones
615 of the Jurassic Sergi Formation, Reconcavo Basin, northeastern Brazil, *in* Houseknecht, D.W.,
616 and Pittman, E.W., eds., Origin, Diagenesis, and Petrophysics of Clay Minerals in Sandstones:
617 SEPM, Special Publication 47, p. 197-208.
618 MU, N., SCHULZ, H.-M., FU, Y., SCHOVSBO, N.H., WIRTH, R., RHEDE, D., AND VAN BERK, W., 2015, Berthierine
619 formation in reservoir rocks from the Siri oilfield (Danish North Sea) as result of fluid-rock
620 interactions: part I. Characterization: Marine and Petroleum Geology, v. 65, p. 302-316.
621 ODIN, G.S., 1988, The verdine facies: introduction to the verdine facies, *in* Odin, G.S., ed., Green Marine
622 Clays: Oolitic Ironstone Facies, Verdine Facies, Glaucony Facies and Celadonite-bearing Facies
623 - A Comparative Study, Elsevier, p. 53-56.
624 ODIN, G.S., 1990, Clay mineral formation at the continent-ocean boundary: the verdine facies: Clay
625 Minerals, v. 25, p. 477-483.
626 PAXTON, S., SZABO, J., AJDUKIEWICZ, J., AND KLIMENTIDIS, R., 2002, Construction of an intergranular volume
627 compaction curve for evaluating and predicting compaction and porosity loss in rigid-grain
628 sandstone reservoirs: American Association of Petroleum Geologists, Bulletin, v. 86, p. 2047-
629 2067.
630 PICHAT, A., HOAREAU, G., CALLOT, J.P., AND RINGENBACH, J.C., 2016, Diagenesis of Oligocene continental
631 sandstones in salt-walled mini-basins-Sivas Basin, Turkey: Sedimentary Geology, v. 339, p. 13-
632 31.

633 PITTMAN, E.D., LARESE, R.E., AND HEALD, M.T., 1992, Clay coats: occurrence and relevance to preservation
634 of porosity in sandstones, *in* Houseknecht, D.W., and Pittman, E.D., eds., Origin, Diagenesis
635 and Petrophysics of Clay Minerals in Sandstones: SEPM, Special Publication 47, p. 241-255.
636 RYAN, P., AND REYNOLDS, R., 1996, The origin and diagenesis of grain-coating serpentine-chlorite in
637 Tuscaloosa Formation sandstone, US Gulf Coast: American Mineralogist, v. 81, p. 213-225.
638 SKARPEID, S.S., CHURCHILL, J.M., HILTON, J.P., IZATT, C.N., AND POOLE, M.T., 2017, The Knarr Field: a new
639 development at the northern edge of the North Sea: Geological Society of London, Petroleum
640 Geology Conference series, v. 8, p. 445-454.
641 SMALL, J.S., HAMILTON, D.L., AND HABESCH, S., 1992, Experimental simulation of clay precipitation within
642 reservoir sandstones 1: techniques and examples: Journal of Sedimentary Petrology, v. 62, p.
643 508-519.
644 SMITH, J.T., AND EHRENBERG, S.N., 1989, Correlation of carbon dioxide abundance with temperature in
645 clastic hydrocarbon reservoirs: relationship to inorganic chemical equilibrium: Marine and
646 Petroleum Geology, v. 6, p. 129-135.
647 STRICKER, S., AND JONES, S.J., 2018, Enhanced porosity preservation by pore fluid overpressure and
648 chlorite grain coatings in the Triassic Skagerrak, Central Graben, North Sea, UK, *in* Armitage,
649 P.J., Butcher, A.R., Churchill, J.M., Csoma, A.E., Hollis, C., Lander, R.H., Omma, J.E., Worden,
650 R.H., eds., Reservoir Quality of Clastic and Carbonate Rocks: Analysis, Modelling and
651 Prediction: Geological Society of London, Special Publication 435, p. 321-341.

652 STRICKER, S., JONES, S.J., SATHAR, S., BOWEN, L., AND OXTOBY, N., 2016, Exceptional reservoir quality in HPHT
653 reservoir settings: Examples from the Skagerrak Formation of the Heron Cluster, North Sea,
654 UK: Marine and Petroleum Geology, v. 77, p. 198-215.
655 SUN, Z.X., SUN, Z.L., YAO, J., WU, M.L., LIU, J.R., DOU, Z.Y., AND PEI, C.R., 2014, Porosity preservation due
656 to authigenic chlorite coatings in deeply buried Upper Triassic Xujiahe formation sandstones,
657 Sichuan Basin, Western China: Journal of Petroleum Geology, v. 37, p. 251-267.

658 TAYLOR, T.R., GILES, M.R., HATHON, L.A., DIGGS, T.N., BRAUNSDORF, N.R., BIRBIGLIA, G.V., KITTRIDGE, M.G.,
659 MACAULAY, C.I., AND ESPEJO, I.S., 2010, Sandstone diagenesis and reservoir quality prediction:
660 models, myths, and reality: American Association of Petroleum Geologists, Bulletin, v. 94, p.
661 1093-1132.
662 VAN HOUTEN, F.B., AND PURUCKER, M.E., 1984, Glauconitic peloids and chamositic ooids - favorable
663 factors, constraints, and problems: Earth-Science Reviews, v. 20, p. 211-243.
664 VIROLLE, M., BRIGAUD, B., LUBY, S., PORTIER, E., FÉNIÈS, H., BOURILLOT, R., PATRIER, P., AND BEAUFORT, D., 2019,
665 Influence of sedimentation and detrital clay grain coats on chloritized sandstone reservoir
666 qualities: Insights from comparisons between ancient tidal heterolithic sandstones and a
667 modern estuarine system: Marine and Petroleum Geology, v. 107, p. 163-184.
668 VIROLLE, M., FÉNIÈS, H., BRIGAUD, B., BOURILLOT, R., PORTIER, E., PATRIER, P., BEAUFORT, D., JALON-ROJAS, I.,
669 DERRIENNIC, H., AND MISKA, S., 2020, Facies associations, detrital clay grain coats and
670 mineralogical characterization of the Gironde estuary tidal bars: A modern analogue for
671 deeply buried estuarine sandstone reservoirs: Marine and Petroleum Geology, v. 114, p.
672 104225.
673 WALDERHAUG, O., LANDER, R., BJØRKUM, P., OELKERS, E., BJØRLYKKE, K., AND NADEAU, P., 2000, Modelling
674 quartz cementation and porosity in reservoir sandstones: examples from the Norwegian
675 continental shelf, *in* Worden, R.H., and Morad, S., eds., Quartz Cementation in Sandstones:
676 International Association of Sedimentologists, Special Publication 29, p. 39-49.
677 WALKER, J.R., 1993, Chlorite polytype geothermometry: Clays and Clay Minerals, v. 41, p. 260-267.
678 WHITE, J.F., TAYLOR, M.C., AND VINCENT, G.P., 1942, Chemistry of chlorites: Industrial & Engineering
679 Chemistry, v. 34, p. 782-792.
680 WOOLDRIDGE, L.J., WORDEN, R.H., GRIFFITHS, J., AND UTLEY, J.E.P., 2017, Clay-coated sand grains in
681 petroleum reservoirs: understanding their distribution via a modern analogue: Journal of
682 Sedimentary Research, v. 87, p. 338-352.

683 WOOLDRIDGE, L.J., WORDEN, R.H., GRIFFITHS, J., AND UTLEY, J.E.P., 2019, How to quantify clay-coat grain
684 coverage in modern and ancient sediments: Journal of Sedimentary Research, v. 89, p. 135-
685 146.
686 WORDEN, R.H., AND MORAD, S., 2000, Quartz cementation in oil field sandstones: a review of the key
687 controversies, *in* Worden, R.H., and Morad, S., eds., Quartz cementation in sandstones:
688 International Association of Sedimentologists, Special publication 29, p. 1-20.
689 WORDEN, R.H., AND BURLEY, S.D., 2003, Sandstone diagenesis: the evolution of sand to stone, *in* Burley,
690 S.D., and Worden, R.H., eds., Sandstone Diagenesis: Recent and Ancient: International
691 Association of Sedimentologists, Special Publication 34, p. 3-44.
692 WORDEN, R.H., AND MORAD, S., 2003, Clay minerals in sandstones: controls on formation, distribution
693 and evolution, *in* Worden, R.H., and Morad, S., eds., Clay Mineral Cements in Sandstones:
694 International Association of Sedimentologists, Special Publication 34, p. 3-41.
695 WORDEN, R.H., ARMITAGE, P.J., BUTCHER, A.R., CHURCHILL, J.M., CSOMA, A.E., HOLLIS, C., LANDER, R.H., AND
696 OMMA, J.E., 2018a, Petroleum reservoir quality prediction: overview and contrasting
697 approaches from sandstone and carbonate communities, *in* Armitage, P.J., Butcher, A.,
698 Churchill, J., Csoma, A., Hollis, C., Lander, R.H., Omma, J., and Worden, R.H., eds., Reservoir
699 Quality of Clastic and Carbonate Rocks: Analysis, Modelling and Prediction: Geological Society
700 of London, Special Publication 435, p. 1-31.
701 WORDEN, R.H., UTLEY, J.E.P., BUTCHER, A.R., GRIFFITHS, J., WOOLDRIDGE, L.J., AND LAWAN, A.Y., 2018b,
702 Improved imaging and analysis of chlorite in reservoirs and modern day analogues: new
703 insights for reservoir quality and provenance, *in* Dowey, P.J., Osborne, M.J., and Volk, H., eds.,
704 Application of Analytical Techniques to Petroleum Systems: Geological Society of London,
705 Special Publication 484.
706 WORDEN, R.H., GRIFFITHS, J., WOOLDRIDGE, L.J., UTLEY, J.E.P., LAWAN, A.Y., MUHAMMED, D.D., SIMON, N., AND
707 ARMITAGE, P.J., 2020, Chlorite in sandstones: Earth-Science Reviews, v. 204, p. 103105.

708 XU, H., AND VEBLEN, D.R., 1996, Interstratification and other reaction microstructures in the chlorite-
709 berthierine series: Contributions to Mineralogy and Petrology, v. 124, p. 291-301.

710

711 **Figure Captions**

712 Fig. 1.---Illustration of the experimental setup. A) Schematic representation of the hydrothermal
713 vessel and its main parts utilized for the diagenesis experiments. The system comprises solely
714 stainless-steel components and a Eurotherm temperature control. B) The interior of the hydrothermal
715 vessel. Approximately 2/3 of the vessel is filled with Na_2CO_3. The meshes including the silica gel and
716 the sandstone sample are attached to the bottom of the sample holder.

717 Fig. 2.---EDS elemental analysis of the Cook Formation (Well 30/6-17R, 2434.8m). A) Montaged
718 electron image of the analyzed sample. Where Ab=albite; Cal = calcite; Kln = kaolinite; Mca = mica; Or
719 = orthoclase; Qtz = quartz; Sd = siderite. B) Elemental distribution. Data reported in weight per cent.
720 C) Increased iron content, important for chlorite precipitation.

721 Fig. 3.---Representative XRD patterns of the Cook Formation (Well 30/6-17R, 2434.8 m) verifying
722 the presence of berthierine. Where Be = berthierine; Chl = chlorite; Kln = kaolinite. A) Overlaid
723 diffractograms of the < 2 mm fraction after the various chemical and heat treatments. The presence
724 of berthierine is indicated by the reduction of intensity of the peak at 25.2 °2θ after the heat treatment
725 at 380° C for 2 h. B) XRD d_{060} reflection allowed the discrimination between chlorite and berthierine.
726 The d_{060} value for berthierine is about 1.555 Å (59.44 2θ°).

727 Fig. 4.---Backscattered electron images (BEIs) showing the different types of berthierine in the
728 sandstone reservoir interval of the Cook Fm (Well 30/6-17R, 2434.8 m). Where Ab = albite; Be =
729 berthierine; Kln = kaolinite; Qtz = quartz; Sd = siderite. A) Ooids made up of concentrically laminated
730 berthierine accreted on a dissolving albite grain. B) Berthierine grain coating. C) Berthierine predates
731 siderite grain coating precipitates. D) Pore filling berthierine and kaolinite booklets.

Fig. 5.---SEM images illustrating the grain-coating nature of berthierine before the hydrothermal experiments. Where Be = berthierine; Kln = kaolinite; Qo = quartz overgrowth; Qtz = quartz; Sd = Siderite. A) Quartz overgrowths interacting with grain-coating berthierine. B) Flake-shaped berthierine detrital crystals. C) Quartz grain partly covered by patchy, discontinuous berthierine coat. D) Siderite growth post-berthierine precipitation but closely associated.

Fig. 6.--- Representative automated mineralogy maps and mineral contact associations. Where Be = berthierine; Chl = chlorite; Other = altered kaolinite, calcite, Fe-Ti oxides, garnet, pyrite, rutile, and unclassified. Porosity values are determined via helium pycnometry. A) Mineral map of the sample treated at 100 °C showing that berthierine concentration is higher than that of chlorite. B) Contact association of berthierine with other minerals and pore space. Note the progressive increase in contact association with chlorite. C) Mineral map illustrating the increased chlorite content of the sample treated at 250 °C. D) Contact association of chlorite with other minerals and pore space. The weak contact with pore space and the strong contact with quartz indicate a higher textural occurrence as coatings. Note the strong association with siderite, a potential source for authigenic chlorite.

Fig. 7.---SEM photomicrographs showing chlorite precipitation and morphology after hydrothermal treatment at 250 °C. A) Partly tangentially oriented, well-developed authigenic chlorite platelets. B) Chlorite grain coating covering a quartz grain. Chlorite develops in a face-to-edge pattern. C) Rosette-like clusters of chlorite. D) Cabbage-head chlorite surrounding well-developed chlorite crystal plates.

Fig. 8.---Siderite dissolution further promotes chlorite authigenesis. Where Cal = calcite; Chl = chlorite; Qtz = quartz; Sd = siderite. Data reported in atomic per cent normalized to oxygen by stoichiometry. A) As temperature increases and dissolution progresses, zonation of siderite due to variations in the Ca, Mg, and Fe content becomes more evident. B) Siderite dissolution and chlorite precipitation around margins of pore space. Chlorite-coating precipitation on the rim of the dissolved crystals. Brighter color in the dissolved crystal represents Fe-dominated areas. Note the increased

757 calcium and magnesium content in the central parts of the crystals as determined by SEM-EDS
758 analysis. C) Chlorite partly engulfing a siderite crystal. D) Siderite crystal undergoing dissolution, hence
759 the hollow cores. Note the presence of calcite crystals, which possibly acted as seeds for siderite
760 development. E) Chlorite precipitation due to siderite decomposition. Note the progressive loss of the
761 rhombohedral morphology of the siderite crystals. The dashed frame corresponds to the outline of a
762 dissolved siderite crystal. F) Authigenic chlorite completely covering a siderite crystal.

763 Fig. 9.---Quantification of berthierine and chlorite content, clay-coat thickness, clay-coat coverage,
764 and porosity with increasing temperature. A) Diagram showing the interdependence of berthierine,
765 chlorite, and siderite. The temperature range for berthierine-to-chlorite transformation is based on
766 the AQM examination and, the siderite's input on chlorite authigenesis is based on SEM imaging. B)
767 Cross-plot of clay coverage against experimental temperatures as determined via Petrog. Highest
768 coverage is observed at temperatures greater than 175 °C. C) Frequency-distribution histogram for all
769 the temperature steps divided by thickness groups as determined via ImageJ. The majority of the
770 thickest coatings are observed at temperatures between 200 °C and 250 °C. C) Porosity evolution as
771 derived by helium pycnometry and jPOR analysis. Porosity reduction is significant between 150 °C and
772 175 °C. Stabilization of porosity is observed at temperatures greater than 175 °C.

773 Fig. 10.---SEM images showing the increase in coat coverage and the main primary porosity
774 reduction mechanism. Where Chl = chlorite; Dck = dickite; Kln = kaolinite; Qtz = quartz; Sd = siderite.
775 A) Clay-free quartz surface before the experiments. B) Initial pore-filling kaolinite with visible
776 microporosity before hydrothermal treatment. C) Chlorite neoformation, promoted by siderite
777 dissolution, on an initial clay-free quartz surface after the hydrothermal experiment at 225 °C. D)
778 Alteration of kaolinite to porosity-occluding dickite.

779 Fig. 11.---Cartoon summarizing the main diagenetic alterations and reservoir-quality evolution of
780 the sandstone samples during the experimental procedure. A) Detrital grains coated by discontinuous
781 berthierine coats and lozenge-shaped siderite crystals. The primary pores are partly filled with

782 kaolinite. B) As temperature increases, cracks in detrital grains, mainly orthoclase, develop and the
783 intergranular pores are progressively filled with dickite, a polymorph of the kaolinite group. Authigenic
784 chlorite starts replacing berthierine. Siderite dissolution begins with individual siderite crystals losing
785 their initial shape and merging together. Chlorite precipitates on precursor-free grain surfaces due to
786 siderite dissolution. C) The conversion of berthierine to chlorite is completed. Further chlorite
787 nucleation is identified on the rims of the dissolving siderite crystals. Hollow cores are prominent,
788 enhancing secondary porosity. Coat coverage is increased with thicker grain coats located mainly next
789 to siderite crystals. Secondary intragranular porosity is generated by the extensive dissolution of
790 albite, which, however, together with mica dissolution promotes further dickitization, hence reducing
791 primary intergranular porosity. D) Chloritization mechanisms of berthierine and siderite with
792 increasing temperature.

793 **Table Captions**

794 Table 1.---Experimental conditions for the hyrothermal reactions. The sandstone (Sst) samples are
795 from the Lower Jurassic Cook Formation of the Oseberg Field (Norway, Well 30/6-17R, 2434.8 m).

796 Table 2.---Bulk rock and clay fraction (, 2 lm) XRD results for the Cook Formation sandstone samples
797 (Well 30/6-17R, 2434.8 m) with the crystallinity of the clay minerals (TR, trace; W, well crystallized; P,
798 poorly crystallized). Data are reported in weight percent.

799 **Figures**

800 Figure 1

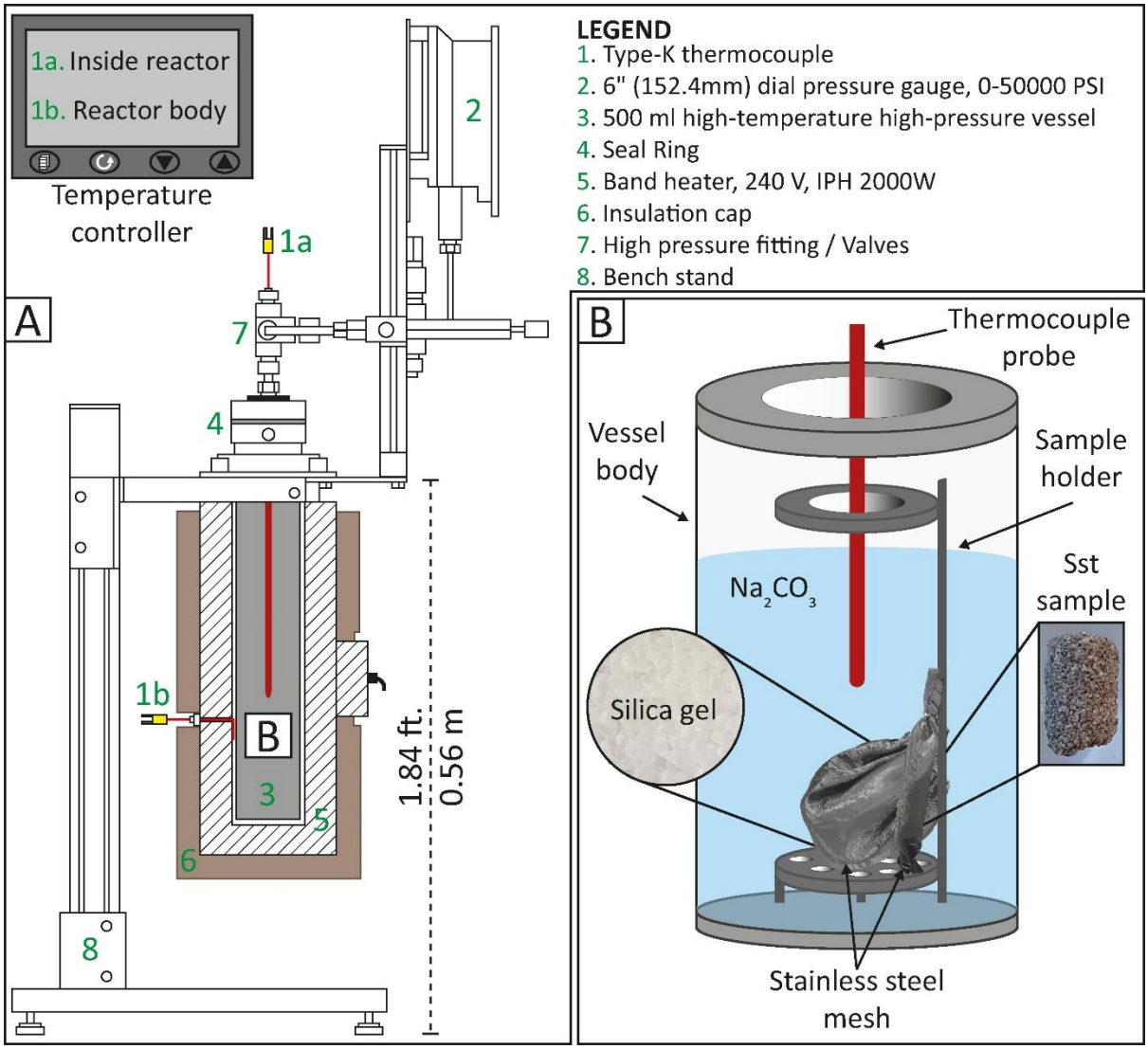

801

802 Figure 2

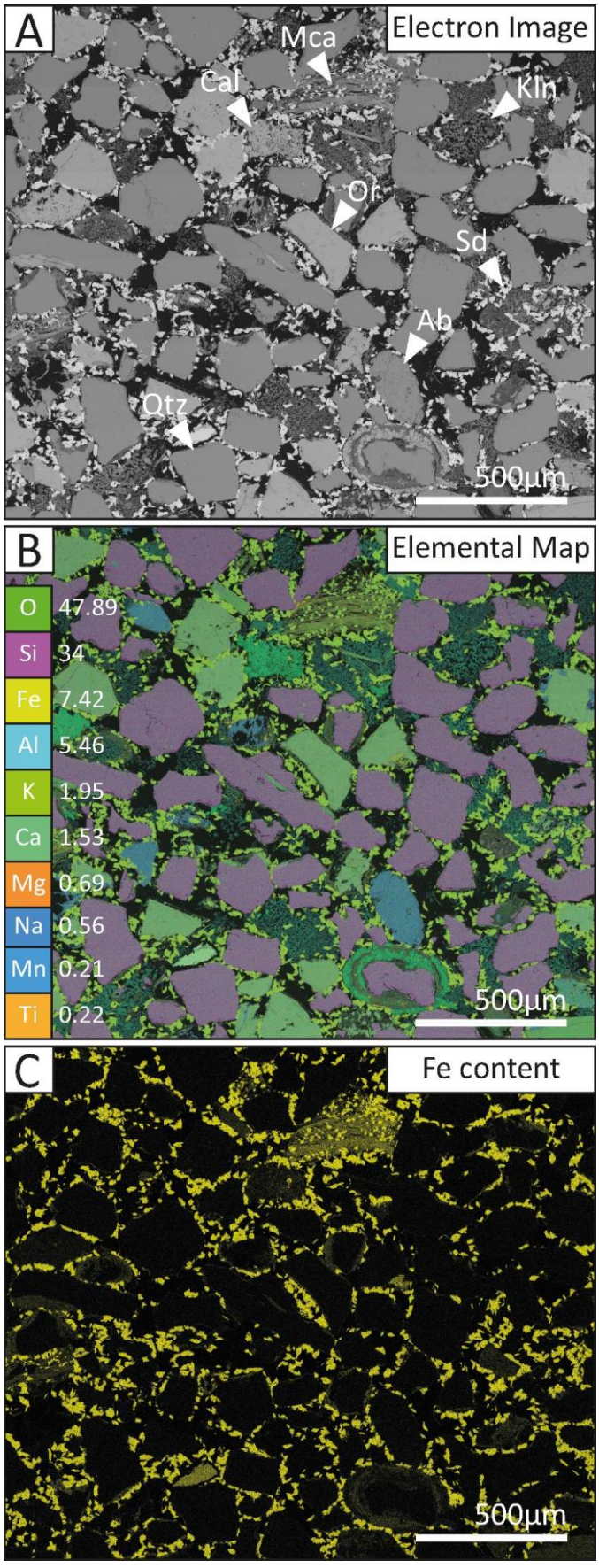

803

804 Figure 3

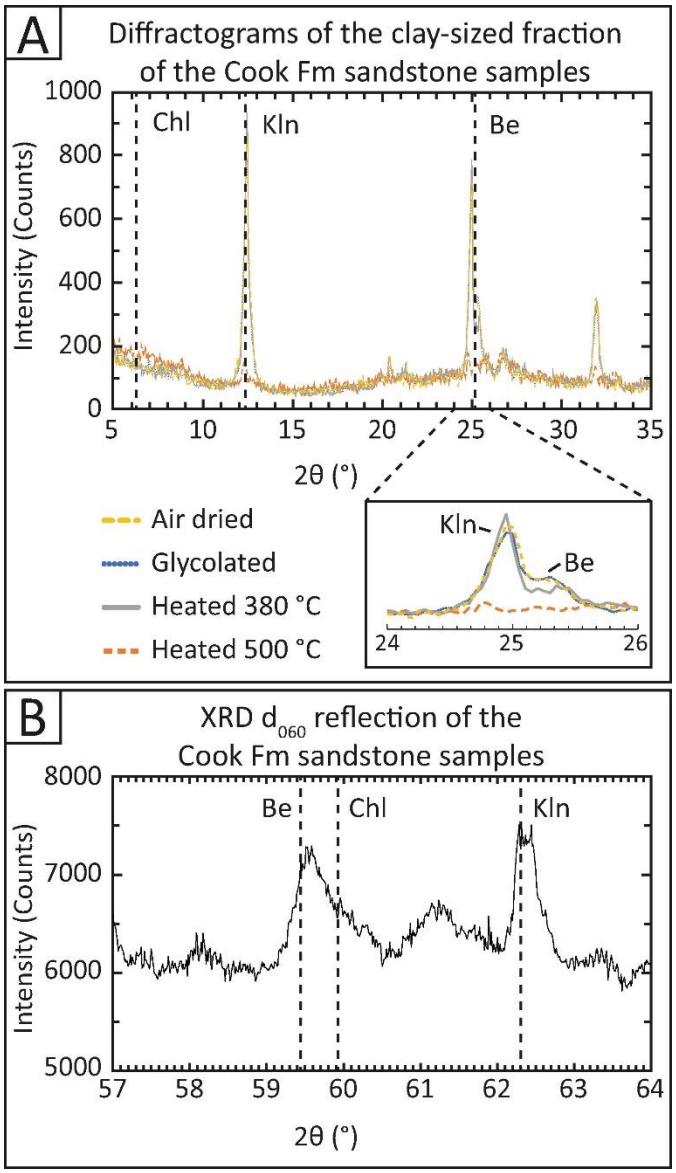

805

806 Figure 4

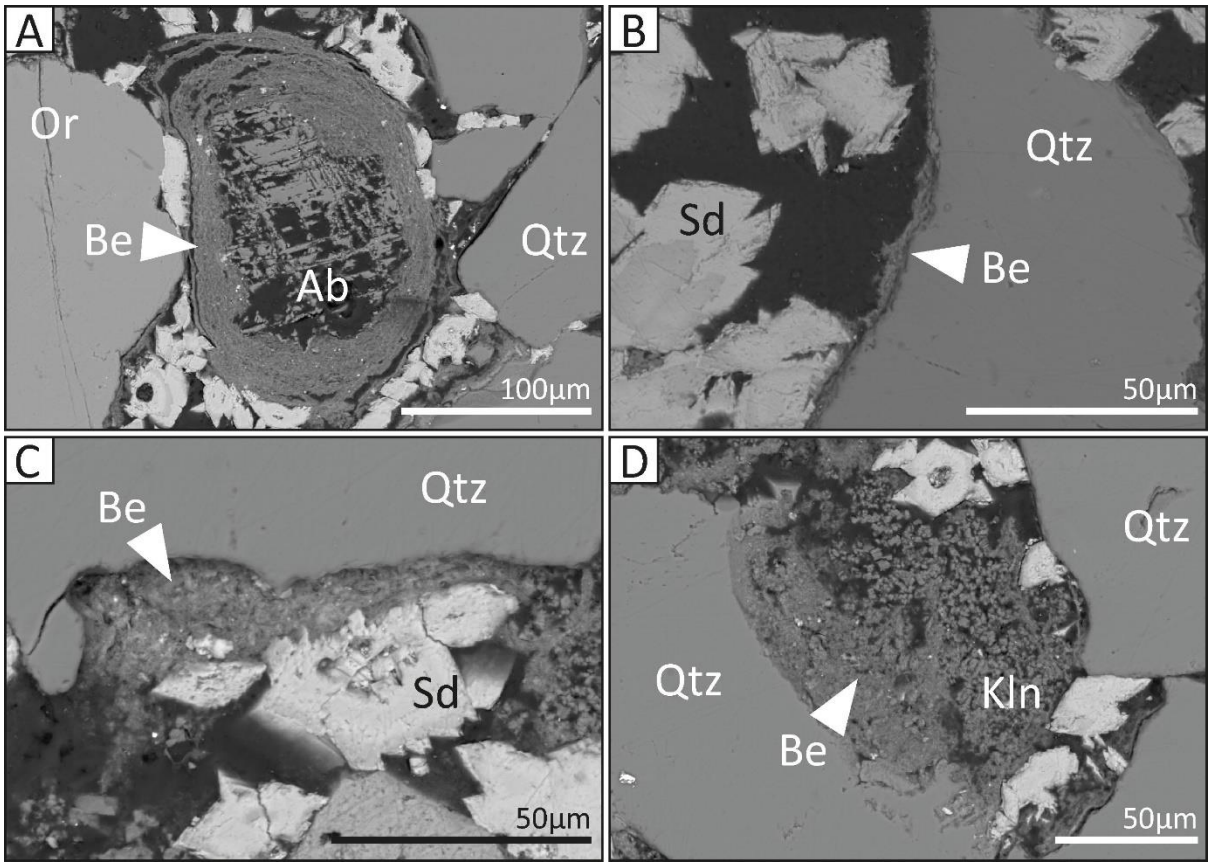

807

808 Figure 5

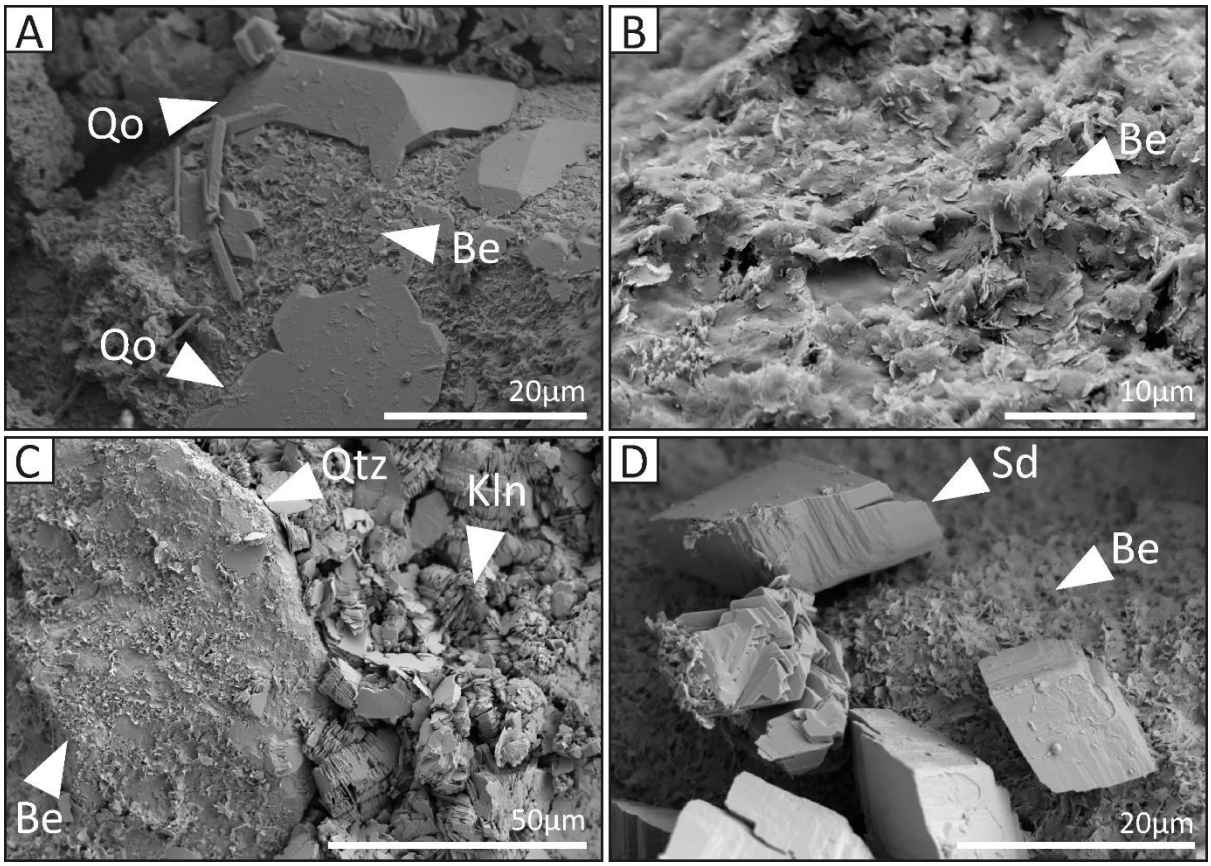

809

Figure 6

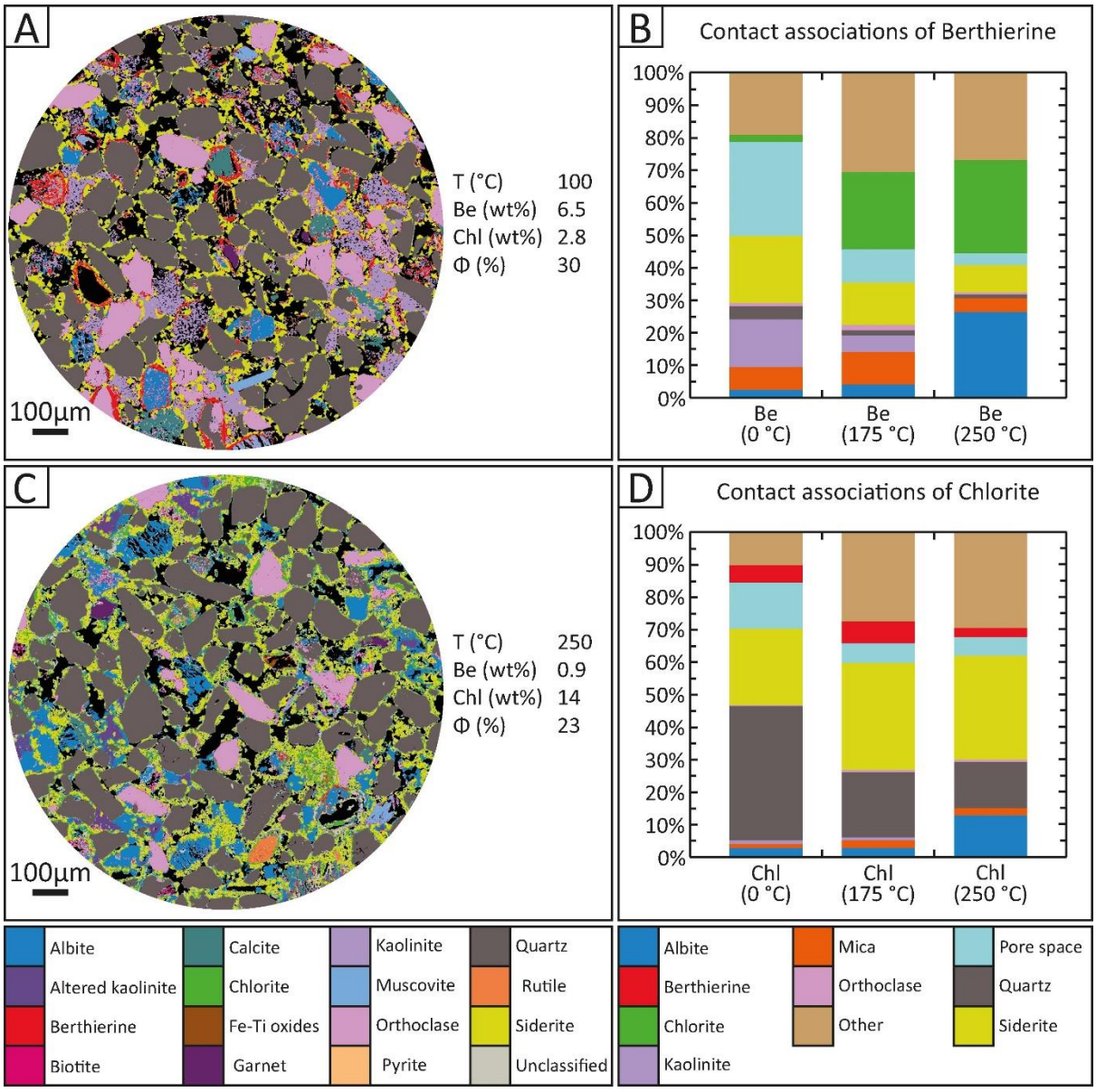
A
T (°C) 100
Be (wt%) 6.5
Chl (wt%) 2.8
Φ (%) 30
100µm
B
Contact associations of Berthierine
100%
90%
80%
70%
60%
50%
40%
30%
20%
10%
0%
Be (0 °C)
Be (175 °C)
Be (250 °C)
C
T (°C) 250
Be (wt%) 0.9
Chl (wt%) 14
Φ (%) 23
100µm
D
Contact associations of Chlorite
Chl (0 °C)
Chl (175 °C)
Chl (250 °C)
Albite
Altered kaolinite
Berthierine
Biotite
Calcite
Chlorite
Fe-Ti oxides
Garnet
Kaolinite
Muscovite
Orthoclase
Pyrite
Quartz
Rutile
Siderite
Unclassified
Albite
Berthierine
Chlorite
Kaolinite
Mica
Orthoclase
Other
Pore space
Quartz
Siderite

812 Figure 7

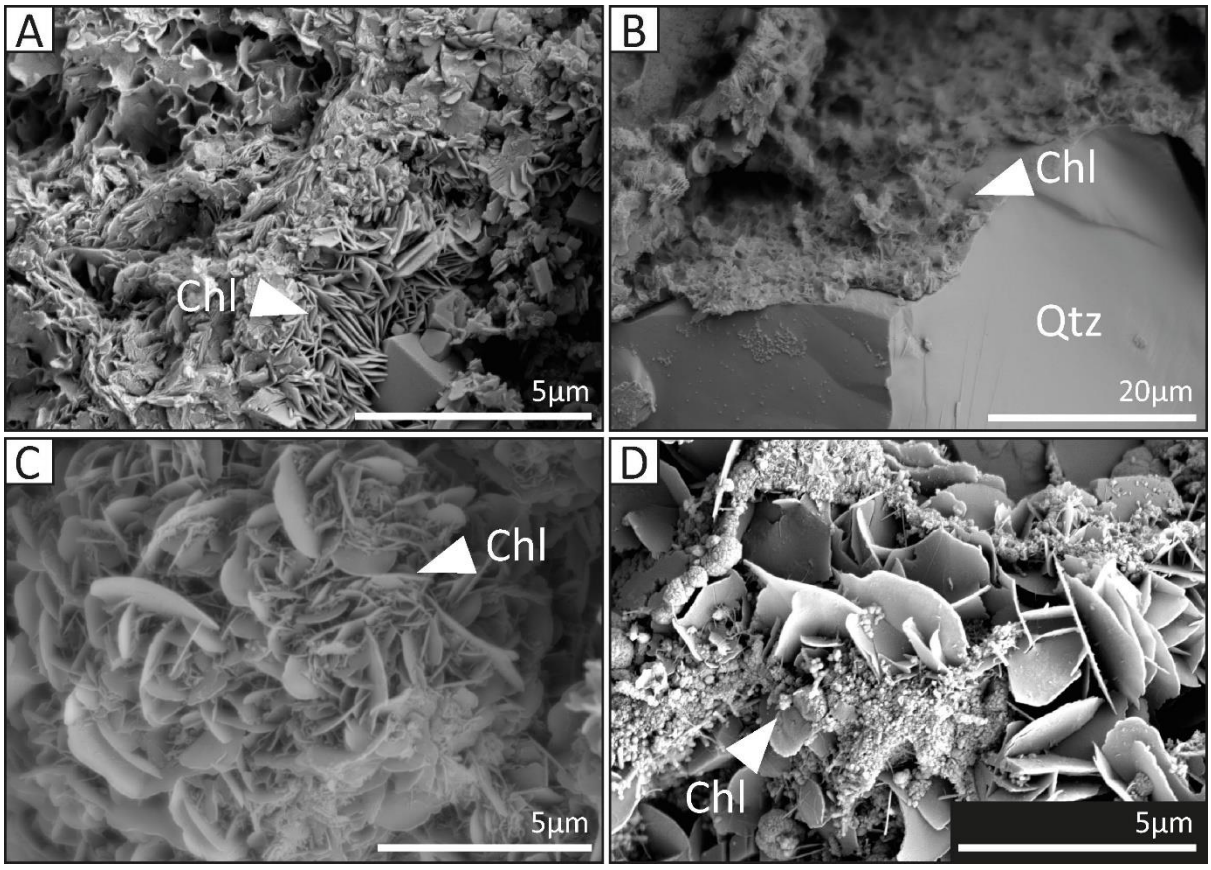

813

814 Figure 8

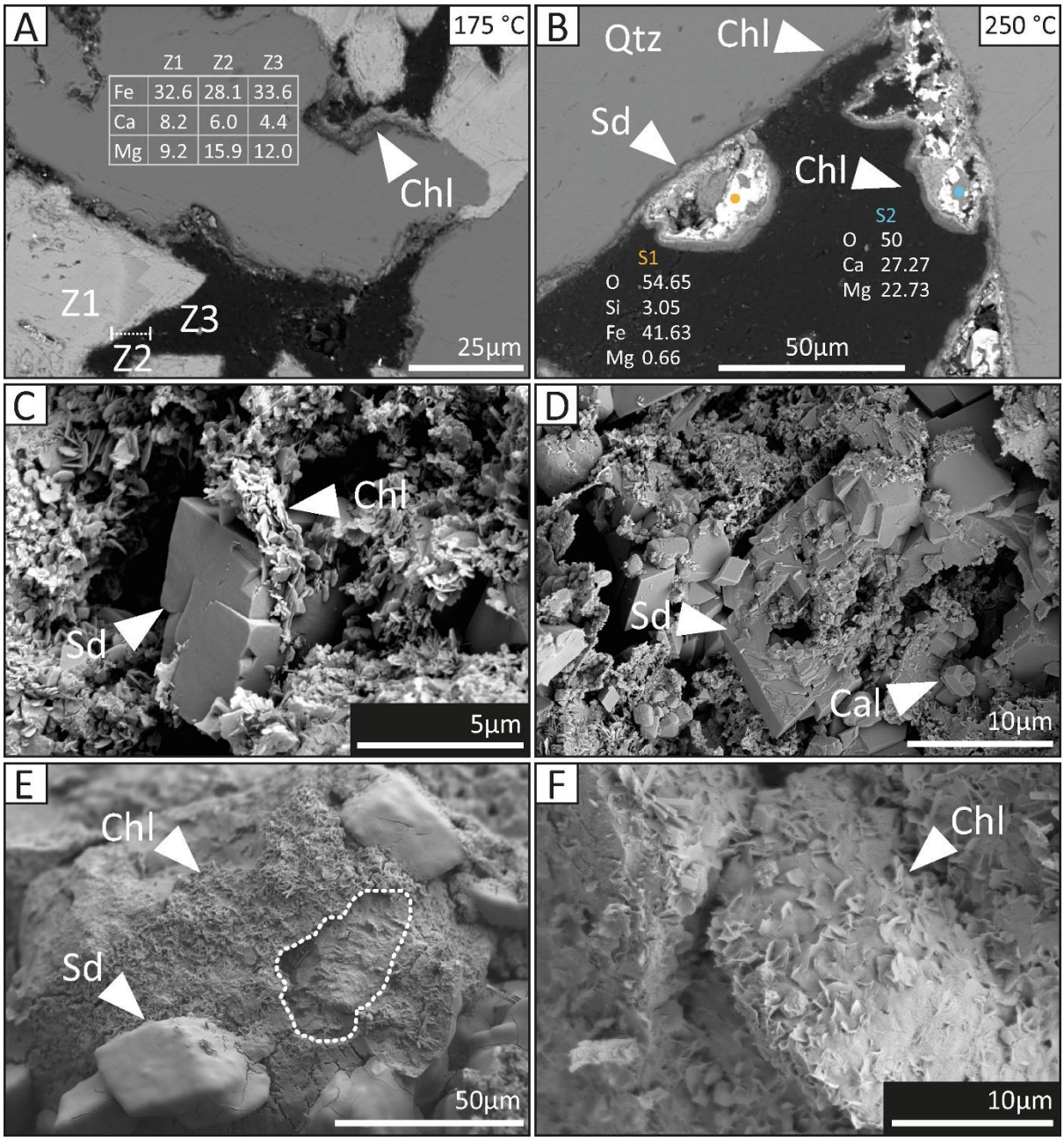

815

Figure 9

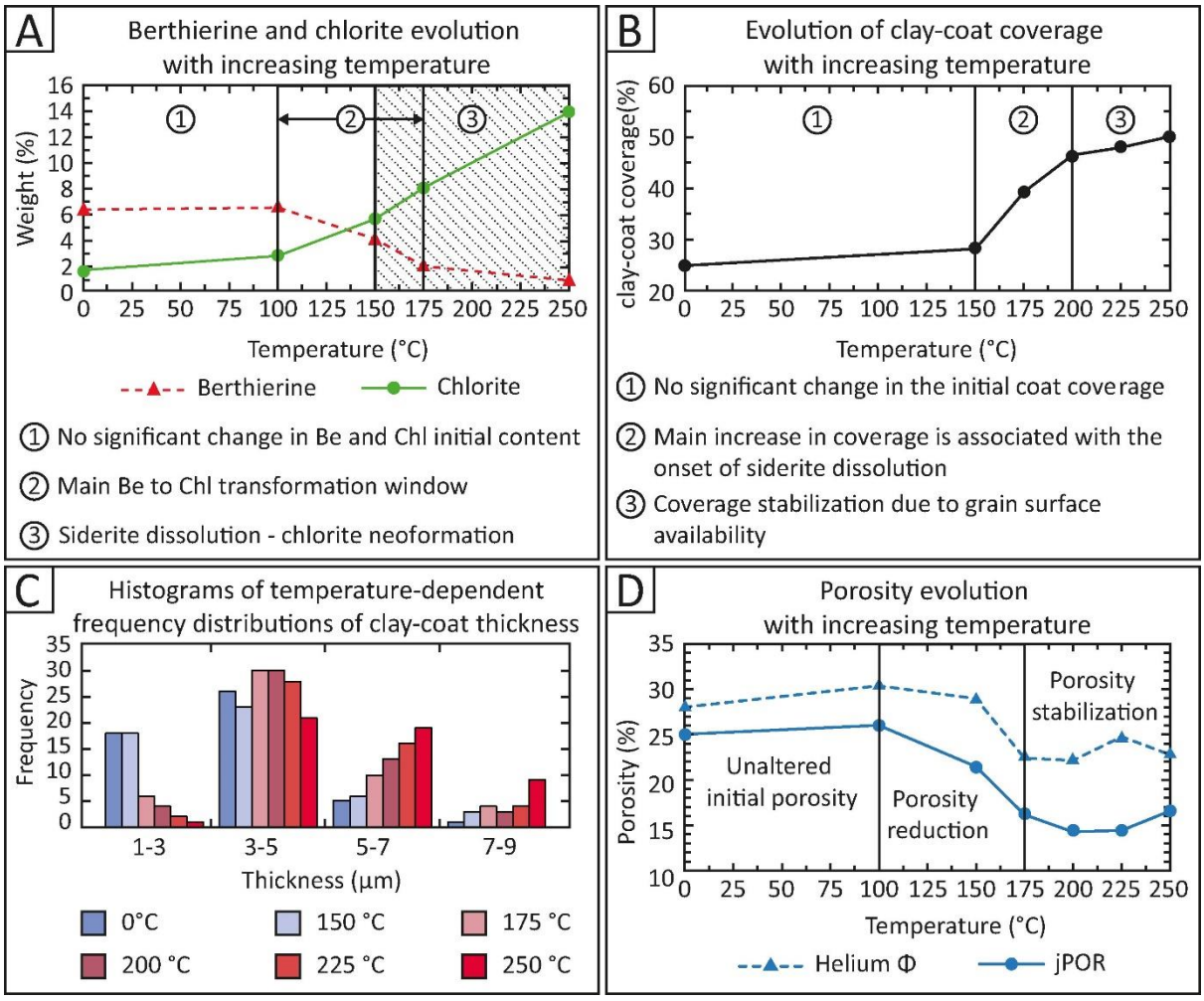
A
Berthierine and chlorite evolution with increasing temperature
Weight (%)
Temperature (°C)
Berthierine
Chlorite
① No significant change in Be and Chl initial content
② Main Be to Chl transformation window
③ Siderite dissolution - chlorite neoformation
B
Evolution of clay-coat coverage with increasing temperature
clay-coat coverage(%)
Temperature (°C)
① No significant change in the initial coat coverage
② Main increase in coverage is associated with the onset of siderite dissolution
③ Coverage stabilization due to grain surface availability
C
Histograms of temperature-dependent frequency distributions of clay-coat thickness
Frequency
1-3
3-5
5-7
7-9
Thickness (µm)
0°C
150 °C
175 °C
200 °C
225 °C
250 °C
D
Porosity evolution with increasing temperature
Porosity (%)
Unaltered initial porosity
Porosity reduction
Porosity stabilization
Temperature (°C)
Helium Φ
jPOR

818 Figure 10

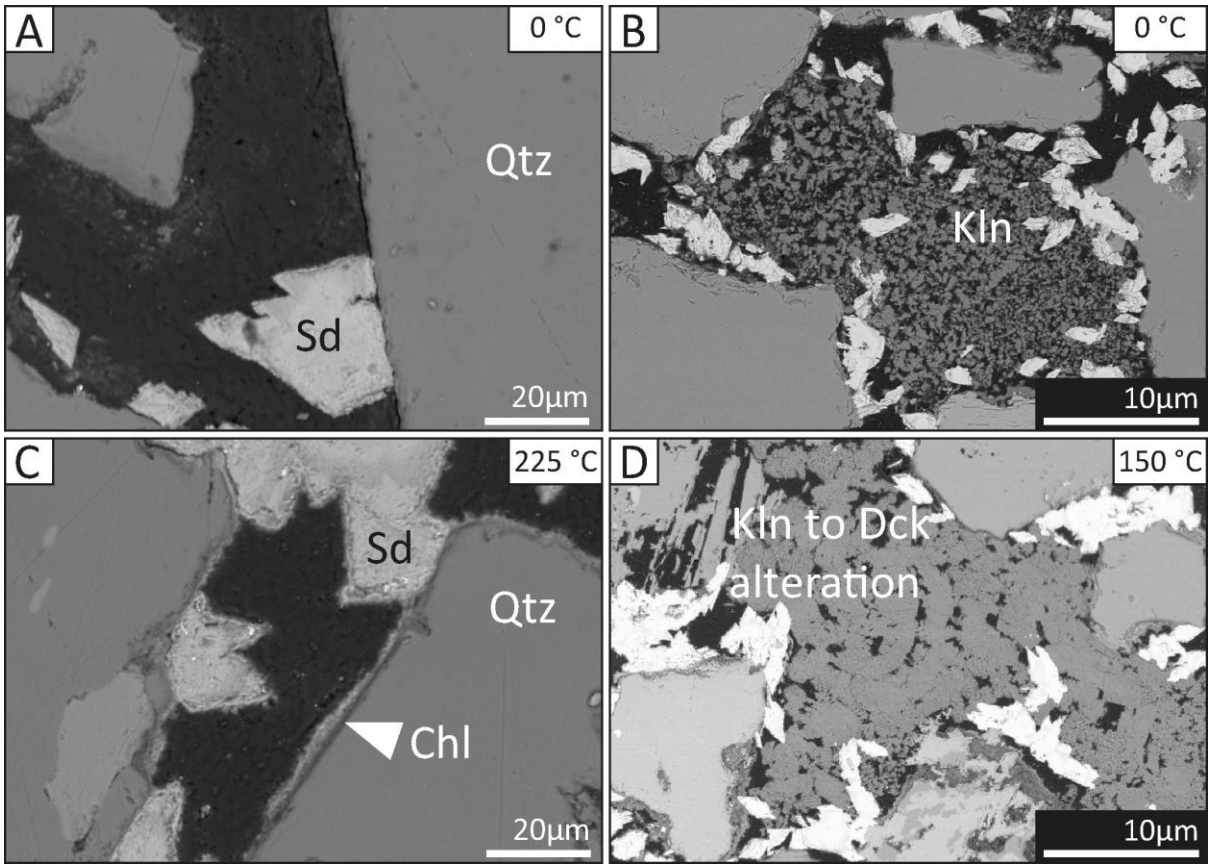

819

820 Figure 11

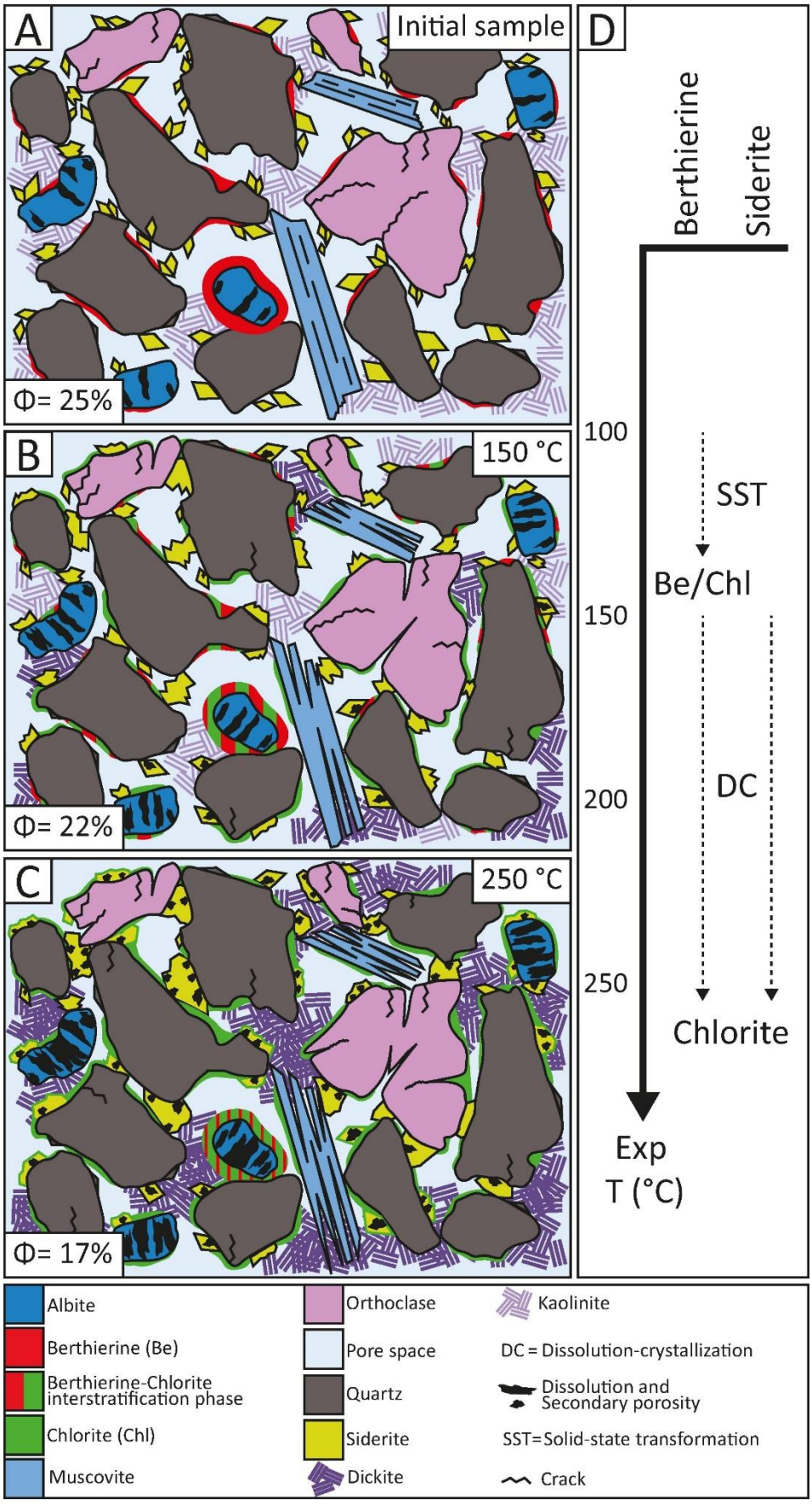

821

822 **Tables**

823 Table 1

Experiment	Sample	Solution (M)	Temperature (°C)	Duration (h)
1	Sst + silica gel	0.1 Na_2CO_3	100	72
2	Sst + silica gel	0.1 Na_2CO_3	150	72
3	Sst + silica gel	0.1 Na_2CO_3	175	72
4	Sst + silica gel	0.1 Na_2CO_3	200	72
5	Sst + silica gel	0.1 Na_2CO_3	225	72
6	Sst + silica gel	0.1 Na_2CO_3	250	72

824

825 Table 2

Minerals	Illite–Smectite	Kaolinite	Chlorite	Berthierine	Quartz	Mica	K-Feldspar	Plagioclase	Calcite	Dolomite	Siderite
Bulk	TR	8.9	0.0	11	48	6.9	4.8	3.1	1.2	0.9	15.6
<2µm	TR	70/W	TR/P	29/P	1	-	-	-	-	-	-

826